The mechanism of Fe-rich intermetallic compound formation and growth on inoculants revealed by electron backscattered diffraction and X-ray imaging

Shikang Feng [a,*], Zelong Jin [b,1], Wenjia Du [c], Insung Han [a], Andrew Lui [a], Xiaorong Zhou [b], Paul R. Shearing [c], Patrick S. Grant [a,*], Enzo Liotti [a,*]

[a] Department of Materials, University of Oxford, Oxford OX1 3PH, UK
[b] Corrosion and Protection Centre, School of Materials, The University of Manchester, Manchester M13 9PL, UK
[c] The Electrochemical Innovation Laboratory, Department of Chemical Engineering, University College London, London WC1E 7JE, UK

HIGHLIGHTS

- The paper concerns a new compositional design approach to make aluminium alloys more recyclable.
- As a possible route to gaining greater control of Fe-rich intermetallic compound formation in recycled Al alloys, the formation and growth of $Al_{13}Fe_4$ intermetallics on of Al_3Ti inoculants are studied systematically in high Fe-containing Al alloys, combining electron backscattered diffraction and X-ray imaging.
- Crystallographic orientation relationships between $Al_{13}Fe_4$ and Al_3Ti are analysed comprehensively, and the formation and growth dynamics of $Al_{13}Fe_4$ on Al_3Ti is also unveiled.
- A strong link is revealed between the formation of $Al_{13}Fe_4$ on Al_3Ti and a twinning-related pseudo-symmetry of $Al_{13}Fe_4$.
- A potential strategy to refine both Fe-rich intermetallics and α-Al in recycled alloys with elevated Fe concentration is proposed for more Fe-tolerant alloy recycling.

GRAPHICAL ABSTRACT
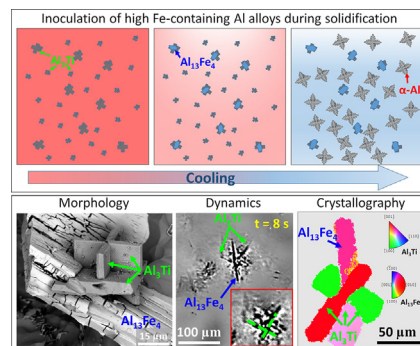
ABSTRACT

Fe-rich intermetallics affect critically the mechanical properties and recyclability of aluminium alloys. Increasing effort has been spent on the inoculation of these intermetallics, hoping to promote a finer distribution. Recently Al-5Ti-1B (wt.%), originally developed to refine α-Al, has been shown to refine $Al_{13}Fe_4$, an intermetallic phase present in a variety of Al alloys. However, mechanisms of the formation and

---

* Corresponding author.
E-mail addresses: shikang.feng@materials.ox.ac.uk (S. Feng), enzo.liotti@materials.ox.ac.uk (P.S. Grant), patrick.grant@materials.ox.ac.uk (E. Liotti).
[1] Current affiliation: Innoval Technology Limited, Beaumont Cl, Banbury OX16 1TQ, UK.

growth of the intermetallics on the inoculants are unclear. In this paper, Ti is added to Fe-containing Al alloys to produce a large number of potent Al_3Ti particles, the active inoculant in Al-5Ti-1B. We use a combination of electron backscattered diffraction, *in situ* synchrotron X-ray radiography and post-solidification X-ray computed tomography to investigate the formation and growth of primary $Al_{13}Fe_4$ on Al_3Ti inoculants, first in a model Al-Fe alloy, with key insights then confirmed in a high Fe-containing, recycled 6xxx alloy. Crystallographic orientation relationships between $Al_{13}Fe_4$ and Al_3Ti are analysed comprehensively, and the formation and growth dynamics of $Al_{13}Fe_4$ on Al_3Ti is also unveiled. A strong link is revealed between the formation of $Al_{13}Fe_4$ on Al_3Ti and a twinning-related pseudo-symmetry of $Al_{13}Fe_4$. Finally, a potential strategy to refine both intermetallics and α-Al in recycled alloys with elevated Fe concentration is proposed.

1. Introduction

In engineering Al alloys, it is principally the minority intermetallic phases that control critically the alloy mechanical properties and corrosion performance [1–4]. Fe-rich intermetallic compounds (IMCs) are an important feature of most Al alloys [5–13]. Due to a large difference between Fe solubility in liquid Al (5 wt.% at 800°C) and solid Al (less than 0.05 wt.%) [14] and the ubiquity of Fe in alloy feedstocks, especially when recycled, Fe precipitates as Fe-rich IMCs during solidification, generally in coarse (typically in the range of ~50 μm to several millimetres [2]), anisotropic morphologies. These IMCs, such as θ-$Al_{13}Fe_4$, α-Al_{15}(Fe, Mn)$_3Si_2$ and β-Al_5FeSi, can act as stress concentrators and degrade the alloy ductility and toughness if their size and shape are not appropriately controlled, usually by solid-state thermomechanical processing [1–3]. Meantime, accumulation of Fe hinders repeated end-of-life alloy recycling. As a result, Al recycling to date has relied heavily on the addition of virgin Al produced by energy- and carbon-intensive smelting process to constrain the Fe concentration, with associated penalties of energy consumption, carbon and other emissions, and logistical costs [1].

Amongst the Fe-rich IMCs, $Al_{13}Fe_4$ is frequently the first Fe-rich phase to form during solidification in a range of engineering Al alloys, such as 2xx and 3xx cast alloys [15,3,16], and 5xxx and 6xxx wrought alloys [4,17,18]. In the widely used Si-containing Al alloys, such as 3xx and 6xxx alloys, $Al_{13}Fe_4$ generally forms at higher temperatures and transforms to α- and/or β-AlFeSi via quasi-peritectic reactions [3,19,16–18], with the orientation of α- and β-AlFeSi dictated by growth behaviour on the $Al_{13}Fe_4$ crystal [17,19,16]. Consequently, the formation of $Al_{13}Fe_4$ strongly affects the size and distribution of subsequent AlFeSi phases. Manipulation of the formation and growth of $Al_{13}Fe_4$ may therefore offer opportunities to gain an extra degree of freedom in controlling the overall species, size and distribution of Fe-rich IMCs in engineering alloys, which may help promote closed-loop alloy recycling. Most work to date has focused on modification of the final IMC phase selection and growth directly, for example by adding transition metals such as Mn, Cr and Co [20–23], or rare earth elements such as Y, La and Ce [20,24,25].

Inspired by the inoculation of α-Al and particularly its ease of operation - small additions (0.01 to 0.5 wt% [26]) of inoculant-containing master alloys such as Al-5Ti-1B (wt.%) change otherwise coarse, elongated columnar α-Al grains (up to centimetres) to a fine (< 100μm), equiaxed grain morphology [27,28] - the inoculation of Fe-rich IMCs has also been explored [29–31]. In an earlier, related work, Lui et al. observed frequent co-location between TiB_2 particle clusters and secondary β-AlFeSi IMCs, suggesting that the formation of β-AlFeSi IMCs may typically be initiated by TiB_2 particles [31]. With the advent of high-energy, high-brilliance synchrotrons and better laboratory-based X-ray sources, together with more efficient X-ray detectors, X-ray imaging techniques have been increasingly used to investigate solidification features in real time, such as crystal formation and growth [32,33], crystal fragmentation [34,35] and thermo-solutal convection [36,37]. As part of these studies, *in situ* X-ray imaging is used to study the dynamics of Fe-rich IMC formation and the effect of inoculant additions [38,9,11], for example the effect of Al-5Ti-1B additions on primary $Al_{13}Fe_4$ formation in hypereutectuc Al-Fe alloys [38,9]. Using synchrotron X-ray radiography, Feng et al. [38] and later other researchers [9] observed a consistent increase in the number density and formation rate of primary $Al_{13}Fe_4$ crystals when Al-5Ti-1B was added to Al-Fe alloys, at a range of solidification conditions.

The commonly used Al-5Ti-1B master alloy contains Al_3Ti particles and TiB_2 particles coated with a nano-scale Al_3Ti-type structure, with Al_3Ti having better wetting with the Al melt and a more potent nucleant for α-Al than TiB_2 [39–41,27,42]. Despite Al-5Ti-1B also being promising to promote the refinement of $Al_{13}Fe_4$ and other similar Fe-rich IMC crystals [31,38,9], its detailed role in IMC formation is so far obscure.

In this paper, we present a new compositional design concept to enhance the impurity compatibility and hence recyclability of Al alloys. A model Al-3Fe (wt.%) alloy was first used, to simulate a high Fe-containing recycled alloy, with additions of 0.7 wt.% Ti. The Al-3Fe-0.7Ti alloy forms primary Al_3Ti (inoculant) at a higher temperature and then $Al_{13}Fe_4$ (IMC of interest), directly from the liquid, and finally α-Al. Al_3Ti inoculants are introduced to the alloy melt via direct additions of Ti rather than Al-5Ti-1B, because Al-5Ti-1B contains only a very small amount (~0.5% [13,43]) of Al_3Ti (and/or Al_3Ti-coated TiB_2) particles that are sufficiently large to serve as potent nucleants for the IMCs.

Electron backscattered diffraction (EBSD), *in situ* synchrotron X-ray radiography and post-solidification X-ray computed tomography (X-ray CT) are combined to study the formation and growth of primary $Al_{13}Fe_4$ IMCs on pre-existing Al_3Ti inoculants. EBSD is used to investigate the orientation relationships (ORs) of 163 Al_3Ti - $Al_{13}Fe_4$ pairs, and the lattice misfit calculated from the ORs showed good agreement with an analytical epitaxial nucleation model. Direct observation of $Al_{13}Fe_4$ formation and growth on Al_3Ti is provided by *in situ* X-ray radiography, and is quantified by post-solidification X-ray CT analysis.

Beyond the model alloy system, the wider applicability of using Al_3Ti to inoculate IMC formation is then confirmed in a recycled 6xxx alloy with a relatively high Fe concentration.

Unlike recent works on IMC inoculation [31,38] that were indirect studies based on either qualitative, post-solidification observation of physical contact between IMCs and inoculants [31] or imaging of IMC formation rate without and with inoculants but could not resolve the inoculants themselves [38], the current work presents *direct*, time-resolved evidence for IMC formation and growth on inoculant particles. We introduce a *semi-quantitative* description of IMC formation tendency on inoculants. Further, unlike previous work we present detailed OR and lattice misfit data based on a large dataset of low-symmetry Fe-rich IMCs and show for the first time the role of twinning-related pseudo-symmetry

in the nucleation of Fe-rich IMCs. Finally, we provide a methodology for exploring more efficient inoculants for $Al_{13}Fe_4$ and other deleterious IMCs that may ultimately assist the development of more impurity tolerant alloys and processes.

2. Experimental methods

2.1. Sample preparation

A model Al-3Fe (wt.%) alloy with 0.7wt.% Ti additions was chosen in which Al_3Ti and then $Al_{13}Fe_4$ formed from liquid. Under equilibrium conditions, Al_3Ti forms at 825°C, and $Al_{13}Fe_4$ starts to form at 710°C. Thermodynamic calculation of the phase fraction as a function of temperature is provided in Fig. S1 in the supplementary materials (SM). Table 1 summaries the techniques used to prepare the alloy ingot and samples for different types of characterisation, and it also lists the experimental (sample) conditions.

2.1.1. Alloy preparation

The alloy was prepared by vacuum arc melting of Al (99.999%), Fe (99.99%) and Ti (99.99%). First, the chamber of the arc melter (Arc 200, Arcast Inc.) was evacuated to 35 mTorr and then backfilled with Ar. The raw materials were melted and mixed in a water cooled Cu crucible with a W-electrode. The solidified ingot was then flipped within the Cu crucible and remelted four times to promote mixing. The outcome was a cap-shaped ingot of ~100 g, with diameter ~50mm and thickness ~15mm, as shown schematically in Fig. S2 in the SM. This was followed by sample preparation for different types of characterisation.

2.1.2. Electron microscopy

EBSD was used to investigate as-cast samples with a cooling rate estimated at ~5 K s^{-1} by thermal imaging in [44,45] of similar ingot sizes. Note the approximate cooling rate for as-cast alloys was comparable to the range used in the radiography experiments. For verification, EBSD was also performed on alloy samples solidified in radiography experiments (Table 1), with examples of their consistent ORs provided in the SM. Unless otherwise stated, electron images and EBSD maps are acquired for as-cast conditions.

EBSD samples were sectioned from the ingot (part 1 in Fig. S2 in the SM) using wire electro-discharge machining (wire EDM) and mounted in Struers PolyFast hot mounting resin, and then ground

with SiC papers to 4000 grit, followed by polishing with diamond suspension to 1μm and finished with colloidal silica on a nap cloth.

To reveal the 3-D crystal morphology of primary $Al_{13}Fe_4$ and Al_3Ti crystals, samples were prepared in the same procedure, followed by deep etching using a 5% NaOH solution for 1 h at room temperature to dissolve the Al matrix. The sample was then rinsed with ethanol and ultrasonically cleaned in an ethanol bath for 30 min to remove any residual etchant and reaction products.

2.1.3. Synchrotron X-ray radiography

In situ synchrotron X-ray radiography was used to investigate the formation and growth dynamics of $Al_{13}Fe_4$ on pre-existing Al_3-Ti in the Al-3Fe-0.7Ti alloy. Foil samples for radiography were sliced from the ingot (part 2 in Fig. S2 in the SM) using wire EDM. Then samples of 15×8mm and thickness of 200 ± 5 μm were prepared by grinding and polishing to a final surface finish of 1μm. Each sample was encapsulated in an X-ray transparent BN cell (Multi-lab, UK) of 100μm thickness.

2.1.4. X-ray CT

Laboratory-based, post-solidification X-ray CT was used to study in 3-D the proportion of primary $Al_{13}Fe_4$ crystals with embedded Al_3Ti, as an evaluation of the tendency of $Al_{13}Fe_4$ formation on Al_3Ti. To prepare the sample for X-ray CT, a rod of 2 mm diameter was machined from the arc melted ingot (part 3 in Fig. S2 in the SM) using wire EDM.

2.2. Data acquisition and analysis

2.2.1. EBSD

A Zeiss Merlin field emission scanning electron microscope (FE-SEM) fitted with a Bruker e-Flash high-resolution EBSD detector was used for crystallographic investigation. The EBSD system was calibrated using Bruker Esprit 2.3 software for accurate determination of crystal orientation (in the form of Euler angles), pattern centre positions and sample-to-detector distance. Esprit 2.3, together with Matlab V2021b (Mathworks, USA) were used to analyse the ORs between Al_3Ti and $Al_{13}Fe_4$ crystals. The reference structures of Al_3Ti [46] and $Al_{13}Fe_4$ [47] used for pattern indexing are listed in Table 2.

Euler angles measured by EBSD were employed to identify the ORs between Al_3Ti and $Al_{13}Fe_4$, which comprised a pair of parallel planes and a pair of parallel directions on the planes. The planes

Table 1
A summary of the techniques used to prepare the alloy ingot and samples for characterisation, and the experimental (sample) conditions. FSEI: fore-scattered electron imaging. BSEI: backscattered electron imaging. EDM: electro-discharge machining.

Alloy ingot				
Composition				Al-3Fe-0.7Ti
Preparation technique				Arc melting
Dimension (mm)				~50 (Dia.)×15
Samples for characterisation				
Characterisation	EBSD + FSEI	BSEI (deep-etched)	Radiography	Tomography
Sample dimension (mm)	15 × 8 × 1	15 × 8 × 1	15 × 8 × 0.2	2 (Dia.)×5
Preparation	Polishing	Polishing, deep etching	EDM, polishing	EDM
Sample condition	0.25 K s^{-1} to as-cast	As-cast	0.25 to 4 K s^{-1}	As-cast

Table 2
Crystal structures and lattice parameters used to index the EBSD patterns for Al_3Ti and $Al_{13}Fe_4$.

Phase	Space group	Pearson symbol	Lattice parameters						Ref.
			a (Å)	b (Å)	c (Å)	α (°)	β (°)	γ (°)	
Al_3Ti	I4/mmm	tI8	3.854	3.854	8.584	90	90	90	[46]
$Al_{13}Fe_4$	C2/m	mS102	15.492	8.078	12.471	90	107.7	90	[47]

and directions in the ORs should be close-packed or nearly close-packed in order for coherent or partially coherent interfaces to form to minimise the nucleation barrier [48–50]. A detailed description of the procedure for OR identification is provided in section S1.3 in the SM. 71 EBSD maps were acquired under as-cast conditions, containing 163 Al_3Ti particles that were embedded in 79 $Al_{13}Fe_4$ crystals (i.e. 163 Al_3Ti - $Al_{13}Fe_4$ pairs). Because the $Al_{13}Fe_4$ contained multiple twins and the Al_3Ti often sat along or across the twin boundaries, an Al_3Ti crystal can possess different (but interrelated) ORs with multiple twin domains of the $Al_{13}Fe_4$, i.e. one Al_3Ti - $Al_{13}Fe_4$ pair could have multiple ORs. Overall, 340 pairs of near-parallel planes were identified, out of which 335 sets of ORs (98.5%) were successfully identified (i.e. containing both the near-parallel planes and directions). ORs are presented in the form of pole figures of the near-parallel planes and directions.

2.2.2. Fore-scattered electron imaging

Fore-scattered electron (FSE) imaging was performed on EBSD samples, in a standard EBSD set-up, to provide orientation contrast of twin domains in the crystals. FSE images were acquired using colour-based Bruker ARGUS™imaging diodes that were mounted at the bottom edge of the EBSD detector. A schematic to demonstrate the set-up is provided in Fig. S3 in the SM. More details about this technique and the ARGUS imaging system can be found in [51,52].

2.2.3. Synchrotron X-ray radiography

Synchrotron X-ray radiography experiments were carried out at the P05 beamline, PETRA III, Germany, using a bespoke Bridgeman furnace described elsewhere [38,43,11,13]. The rig was operated with a controlled Ar atmosphere to protect foil samples and heating elements from oxidation.

During solidification experiments, foil samples were illuminated with a monochromatic X-ray beam at an energy of 19 keV. The transmitted beam from the sample was collected onto a 200 μm thick LuAG:Ce $(Lu_3Al_5O_{12}:Ce)$ single crystal scintillator, which then projected the image onto a KIT CMOS detector through a $5\times$ objective lens system. Radiography videos were recorded at 10 Hz with an image pixel size of 1.28μm. Overall, 45 solidification experiments were performed under near-isothermal cooling, at cooling rates ranging from 0.25 Ks^{-1} to 4 Ks^{-1}.

2.2.4. Post-solidification X-ray CT

A laboratory-based, W-anode X-ray CT scanner (ZEISS Xradia 620 Versa, Carl Zeiss Inc., Pleasanton, USA) was used to scan the rod sample prepared in Section 2.1.4 at multiple length scales with a polychromatic cone beam X-ray, using a source voltage of 120 kV. The system employs two-stage magnification using conventional geometric magnification and an optically coupled scintillator post transmission, offering variable resolution and field of view depending on the objective lens selection. First, the sample was scanned at a lower magnification of $4\times$ (termed "Mag 1", at a voxel resolution of 2.4μm); 1601 projections were collected during a 180° rotation with an exposure time of 2 s per projection, providing a reconstructed sample volume of 10.4mm³. Second, scans at a higher magnification of $20\times$ were conducted (termed "Mag 2", at a voxel resolution of 0.47μm); 1201 projections were collected during a 180° rotation with an exposure time of 15 s to provide a region-of-interest scan of a smaller volume of 0.1mm³. The projections were then reconstructed and segmentation performed to separate crystals of different phases, i.e. $Al_{13}Fe_4$, Al_3Ti and the α-Al matrix, following a procedure described in section S1.5 in the SM.

The scan at Mag 1 was used to analyse the number of $Al_{13}Fe_4$ crystals that contained Al_3Ti. Each $Al_{13}Fe_4$ crystal in the sample volume was examined slice-by-slice manually for any embedded Al_3Ti crystals. The same process was repeated twice to promote accuracy. The $Al_{13}Fe_4$ and Al_3Ti were easily distinguished by X-ray attenuation contrast. The scan at Mag 2 was used to investigate individual Al_3Ti - $Al_{13}Fe_4$ pairs from different angles, as a complement to deep etching and microscopy.

3. Results

Figs. 1 (a) to (d) show backscattered electron images of Al_3Ti embedded either fully or partially in $Al_{13}Fe_4$ crystals, suggesting that Al_3Ti particles might act as nucleants for $Al_{13}Fe_4$. The light grey phase is $Al_{13}Fe_4$ (denoted as AF), the dark grey phase is Al_3Ti (denoted as AT), and the black phase is Al. More SEM images (including images at lower magnifications) are available in Fig. S4 in the SM. Figs. 1(e) to (h) show FSE images that provide orientation contrast, with twin domains in $Al_{13}Fe_4$ clearly resolved.

Fig. 2 presents an example of the data and methodology for OR identification. In this case, an Al_3Ti and an $Al_{13}Fe_4$ crystal were closely attached to each other, with their preferential growth direction parallel (Fig. 2(a)). Considering that both phases formed as
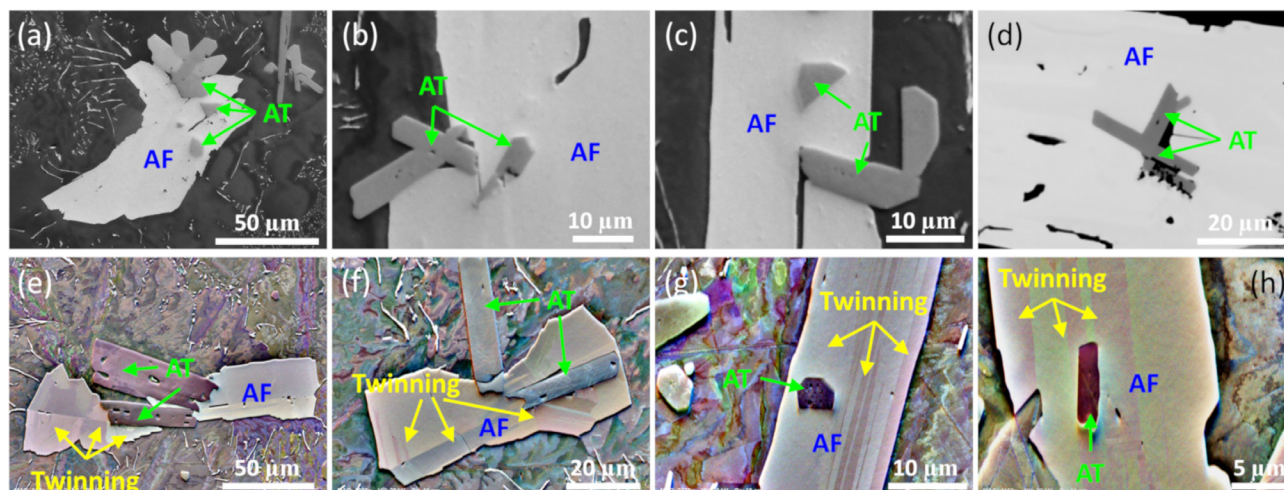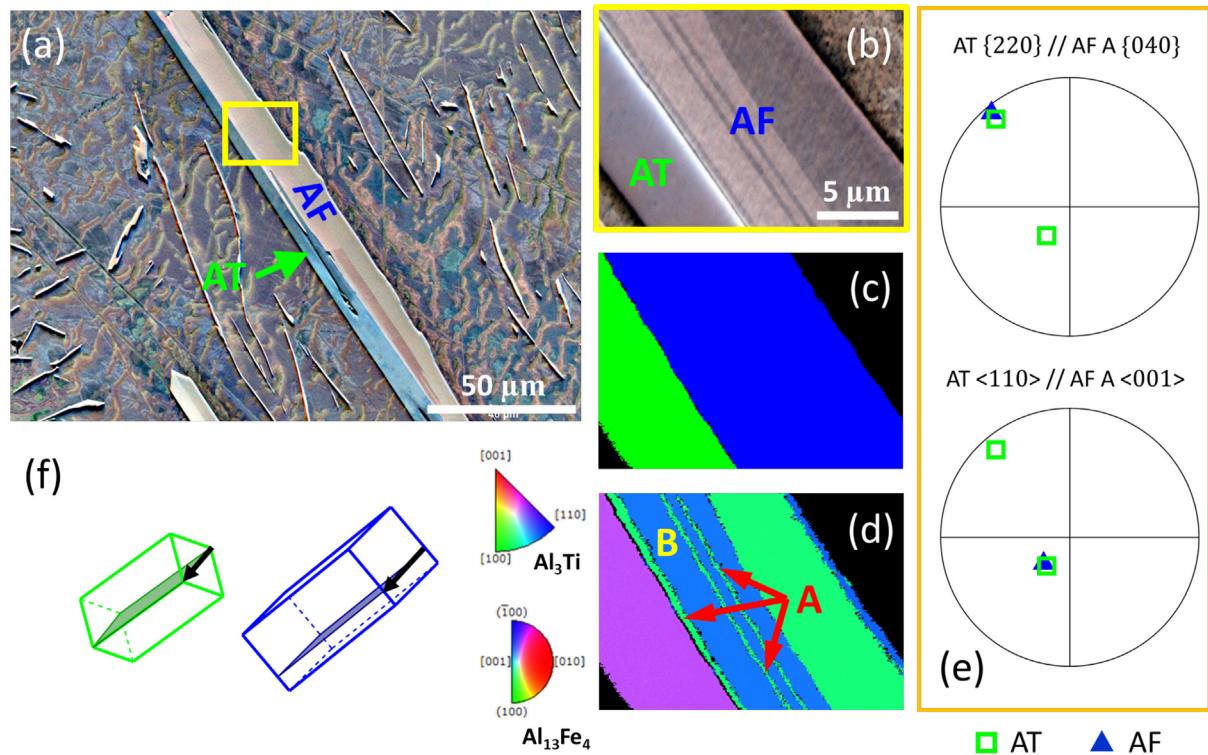

Fig. 1. (a) to (d) Backscattered electron images of Al_3Ti embedded either fully or partially in $Al_{13}Fe_4$ crystals. The light grey phase is $Al_{13}Fe_4$, the dark grey phase is Al_3Ti, and the black phase is Al. (e) to (h) FSE images of Al_3Ti embedded either fully or partially in $Al_{13}Fe_4$, showing orientation contrast. AF: $Al_{13}Fe_4$; AT: Al_3Ti.

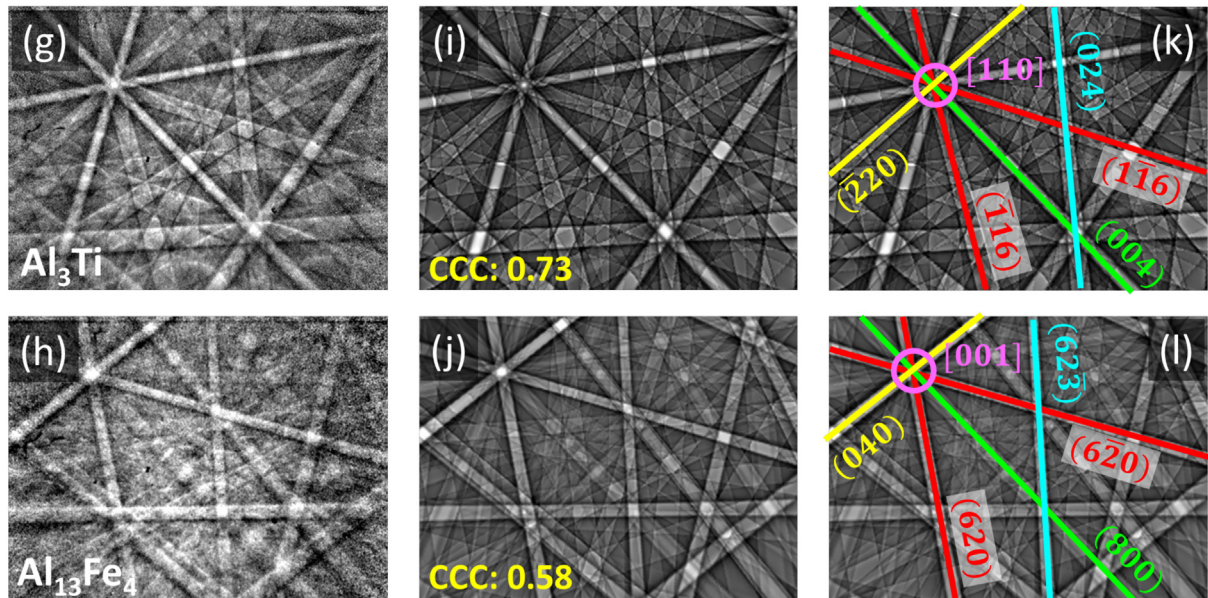**Fig. 2.** (a) An FSE image showing an Al_3Ti crystal (AT) and an $Al_{13}Fe_4$ crystal (AF) closely associated with each other, with parallel preferential growth direction. (b) An FSE image at a higher magnification for the area indicated by an yellow box in (a). (c) An EBSD phase map of the $Al_{13}Fe_4$ and Al_3Ti in (b). The blue phase is $Al_{13}Fe_4$, and the green phase is Al_3Ti. (d) An inverse pole figure colour map (IPF-Z) revealing the orientations of the $Al_{13}Fe_4$ and Al_3Ti crystals. A and B indicate twin domains in the $Al_{13}Fe_4$ crystal. (e) Superimposed pole figures of the near-parallel planes and directions of Al_3Ti and $Al_{13}Fe_4$ (twin A). The green square box in each pole figure indicates the Al_3Ti, and the blue triangle indicates the $Al_{13}Fe_4$. (f) Unit cell wire frames, showing the orientation of the Al_3Ti (green) and its counterpart in the $Al_{13}Fe_4$ (blue). (g) and (h) Experimental EBSD patterns of Al_3Ti and $Al_{13}Fe_4$ (twin A), respectively. (i) and (j) Corresponding dynamical simulation patterns. (k) and (l) The same simulated patterns with the near-parallel planes and zone axes (directions) indexed.

primary phases in free liquid, rather than constrained by any pre-existing solid network, it was likely that the $Al_{13}Fe_4$ with the lower formation temperature formed on pre-existing Al_3Ti (as shown later by *in situ* X-ray radiography). Fig. 2(b) provides a higher magnification view indicated by the yellow box in Fig. 2(a), and emphasises the orientation contrast from twinning. Fig. 2(c) shows an

EBSD phase map, where blue phase is $Al_{13}Fe_4$ and green phase is Al_3Ti. Fig. 2(d) is an inverse pole figure colour map (IPF-Z) revealing the orientation of the $Al_{13}Fe_4$ and Al_3Ti crystals. Fig. 2(d) also shows parallel twin domains (denoted as A and B) in $Al_{13}Fe_4$, with twin A sharing an interface with the Al_3Ti. Following the method described in Section 2.2.1, Fig. 2(e) shows the superimposed pole

figures of the near-parallel planes and near-parallel directions of the Al_3Ti and $Al_{13}Fe_4$. One plane in the {220} family of the Al_3Ti was near-parallel (angular mismatch $\theta = 3.6°$) with the {040} of twin A in the $Al_{13}Fe_4$; and one direction of the ⟨110⟩ family of the Al_3Ti was near-parallel ($\theta = 3.3°$) with the ⟨001⟩ of twin A of the $Al_{13}Fe_4$. For clarity, the orientation of the Al_3Ti crystal and its counterpart in the $Al_{13}Fe_4$ are illustrated by unit cell wire frames in Fig. 2(f), with the near-parallel planes and directions indicated.

To verify the OR, the EBSD patterns of the Al_3Ti and its counterpart in the $Al_{13}Fe_4$ were further analysed by performing cross correlation between the experimental patterns and dynamical simulation patterns using Bruker DynamicS software. Figs. 2(g) and (h) are the experimental patterns for $Al_{13}Fe_4$ and Al_3Ti, and

Figs. 2(i) and (j) show the best-fit simulation patterns, with a cross correlation coefficient (CCC) of 0.73 and 0.58 respectively. A CCC = 1 indicates a perfect fit, and CCC > 0.5 is considered as a good fit for low-symmetry IMCs [53,45]. Figs. 2(k) and (l) reproduce the simulation patterns but now with the near-parallel bands (i.e. planes) and zone axes (i.e. directions) indexed, confirming $\{220\}_{AT}//\{040\}_{AF}$ and $⟨110⟩_{AT}//⟨001⟩_{AF}$, as shown in Fig. 2(e). In addition, Figs. 2(k) and (l) also revealed other less close-packed ORs, which are listed in Table 3. The similarity of the two patterns for Al_3Ti and $Al_{13}Fe_4$ in Figs. 2(k) and (l) is readily apparent.

In comparison with Fig. 2(a), where one Al_3Ti crystal and one $Al_{13}Fe_4$ crystal are parallel sharing a single interface, $Al_{13}Fe_4$ crystals were also frequently associated with more than one Al_3Ti crystal, in a cruciform (orthogonal) configuration. Fig. 3 presents backscattered electron images of the 3-D morphology of deep etched $Al_{13}Fe_4$ and Al_3Ti. Fig. 3(a) shows the microstructure at lower magnification, and Figs. 3(b) to (d) show examples of $Al_{13}Fe_4$ crystals associated with Al_3Ti particles oriented in the orthogonal configuration.

From the 79 Al_3Ti-containing $Al_{13}Fe_4$ crystals studied by EBSD, 49% (39 out of 79) contained at least two orthogonal Al_3Ti crystals, and 24% (19 out of 79) contained a cluster of three orthogonal Al_3Ti crystals.

A further example of this orthogonal configuration is shown in Fig. 4. The FSE image in Fig. 4(a) and the phase map in Fig. 4(b) show multiple Al_3Ti particles embedded (either fully or partially)

Table 3
The ORs identified between Al_3Ti and $Al_{13}Fe_4$ (twin A) in Figs. 2(k) and (l). The close-packed OR is indicated by C.P. OR. * Denotes less close-packed planes or directions involved in the other ORs.

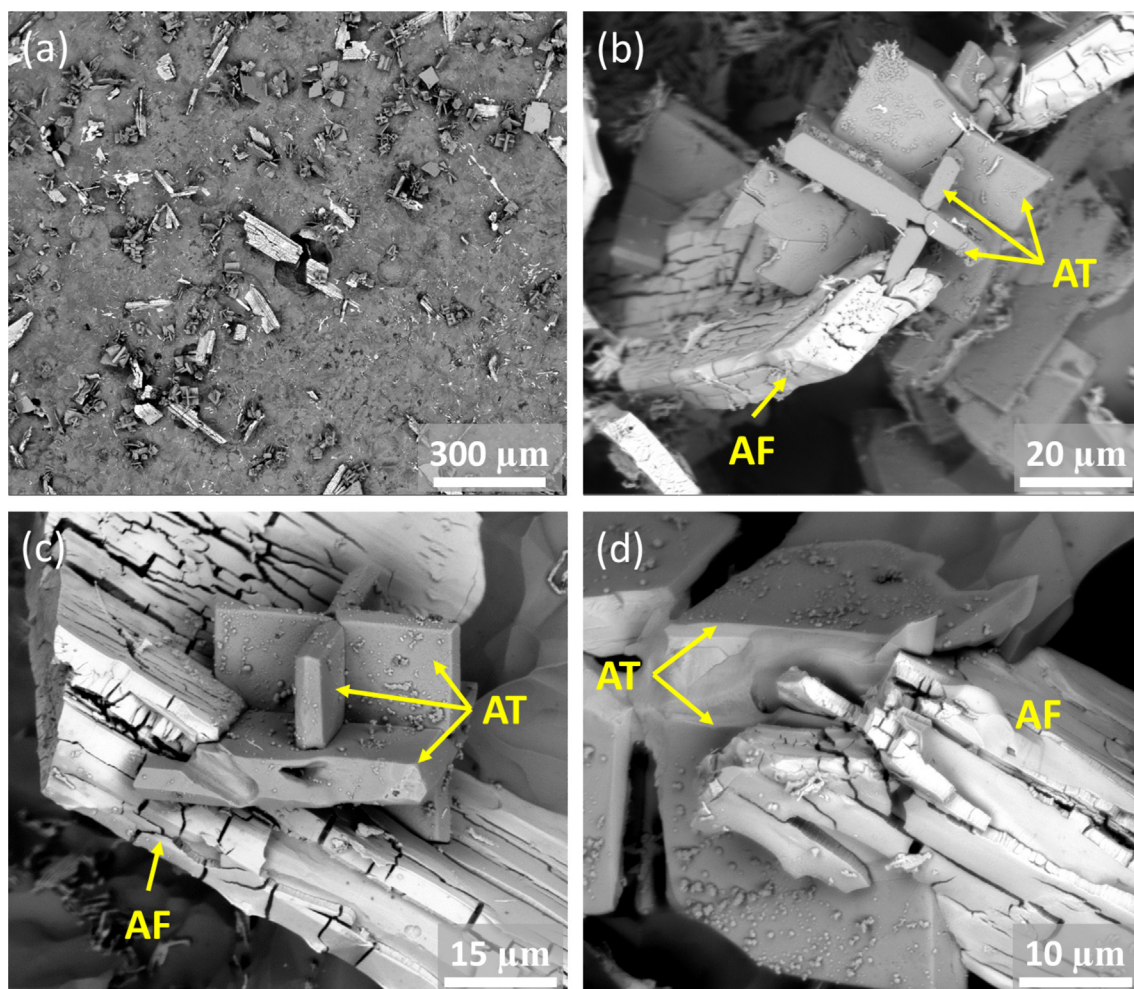|	Parallel planes		Parallel directions	
	AT	AF A	AT	AF A
C.P. OR	{220}	{040}	⟨110⟩	⟨001⟩
Other ORs	{116}*	{620}	⟨110⟩	⟨001⟩
	{004}	{800}*	⟨110⟩	⟨001⟩
	{204}	{623}	⟨221⟩*	⟨102⟩

Fig. 3. (a) A backscattered electron image showing the microstructure of Al-3Fe-0.7Ti in a deep etched condition. (b) to (d) Backscattered electron images showing $Al_{13}Fe_4$ crystals associated with Al_3Ti particles that were orientated in an orthogonal configuration. The light grey phase is $Al_{13}Fe_4$ (AF), and the dark grey phase is Al_3Ti (AT).
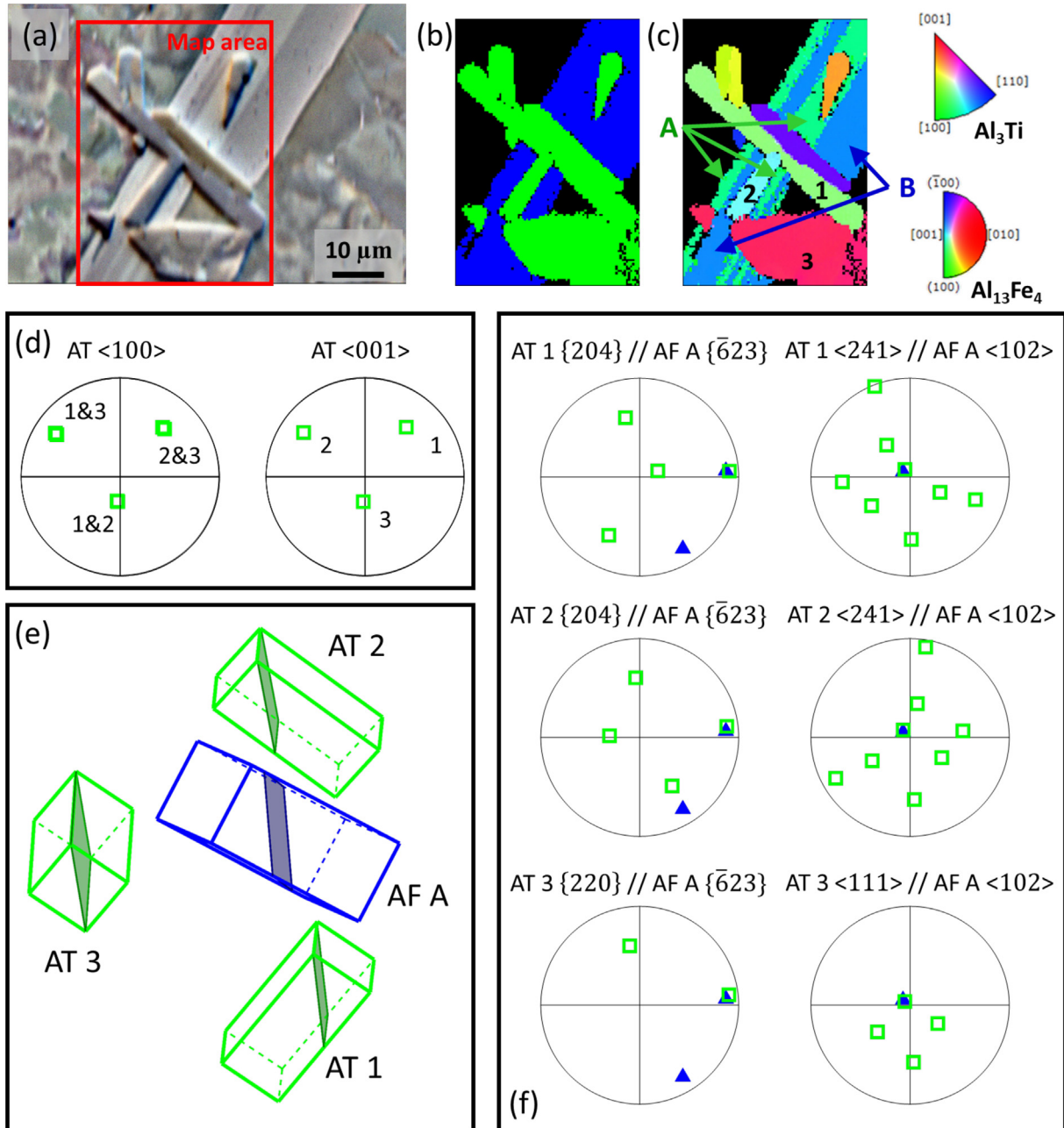
Fig. 4. (a) An FSE image showing an $Al_{13}Fe_4$ crystal associated with multiple Al_3Ti particles. The red box indicates the area of the EBSD maps in (b) and (c). (b) An EBSD phase map of the $Al_{13}Fe_4$ and Al_3Ti crystals in (a). The blue phase is $Al_{13}Fe_4$, and the green phase is Al_3Ti. (c) An inverse pole figure colour map (IPF-Z) revealing the orientations of the $Al_{13}Fe_4$ and Al_3Ti crystals. "1", "2" and "3" denote three Al_3Ti particles that sat in an orthogonal configuration. A and B denote the twins in the $Al_{13}Fe_4$ crystal. (d) Superimposed pole figures of the $\langle 100 \rangle$ and $\langle 001 \rangle$ directions for Al_3Ti particle 1, 2 and 3, confirming an orthogonal arrangement. (e) Unit cell wire frames, showing the orientations of Al_3Ti particle 1, 2, and 3 and the orientation of twin A in the $Al_{13}Fe_4$. The near-parallel planes are highlighted, and the near-parallel directions are approximately perpendicular to the paper. (f) Superimposed pole figures of the near-parallel planes and directions of Al_3Ti particles and twin A of the $Al_{13}Fe_4$.

in an $Al_{13}Fe_4$ plate. "1", "2" and "3" in the IPF-Z (Fig. 4(c)) denote three orthogonal Al_3Ti particles. Meanwhile, similar to Fig. 2(d), Fig. 4(c) again reveals layered twin domains in the $Al_{13}Fe_4$ plate, labelled as "A" (green area) and "B" (light blue area). Superimposed pole figures of the $\langle 100 \rangle$ and $\langle 001 \rangle$ directions for Al_3Ti particles 1, 2 and 3 (Fig. 4(d)) confirmed the orthogonal arrangement: there was a 90° rotation between particles 1 and 2, 2 and 3, and 1 and 3 about their common a-axis, as also illustrated by unit cell wire frames in Fig. 4(e).

ORs were identified between twin A of the $Al_{13}Fe_4$ and Al_3Ti particle 1, 2 and 3, respectively, and they are presented in Fig. 4 (f). The 3 ORs were:

$$\{204\}_{AT1}//\{\bar{6}23\}_{AF}; \ \langle 241 \rangle_{AT1}//\langle 102 \rangle_{AF} \tag{1}$$

$$\{204\}_{AT2}//\{\bar{6}23\}_{AF}; \ \langle 241 \rangle_{AT2}//\langle 102 \rangle_{AF} \tag{2}$$

$$\{220\}_{AT3}//\{\bar{6}23\}_{AF}; \ \langle 111 \rangle_{AT3}//\langle 102 \rangle_{AF} \tag{3}$$

The ORs are illustrated in Fig. 4(e), with the near-parallel planes highlighted, and the corresponding near-parallel directions in this case were approximately perpendicular to the page, as can be noticed from the pole figures in the second column of Fig. 4(f). Furthermore, the ORs above and the wire frames in Fig. 4(e) suggest that near-parallelism existed between {220} of Al_3Ti particle 3

and {204} of Al$_3$Ti particle 1 and 2. This can be ascribed to the body-centred tetragonal (D0$_{22}$) (super) structure of Al$_3$Ti, with $c \approx 2a$ ($c/2a = 1.11$) [46]. The unit cell can be viewed as two face-centred cubic (L1$_2$) cells stacking along the c-axis if assuming $c = 2a$ [54,55].

Further SEM images of Al$_3$Ti in similar arrangements can be found in Fig. S4 in the SM, and more EBSD maps of Al$_{13}$Fe$_4$ containing orthogonal Al$_3$Ti are provided in Fig. S5 of the SM.

An interpretation of the frequently observed orthogonal configuration could be that Al$_3$Ti particles formed on the same nucleation site and grew in such a way to minimise the surface free energy as they formed as a primary phase from the free liquid [56]. A similar observation was reported by St. John and Hogan in 1979, in a hypereutectic Al-Ti alloy studied by SEM [57]. They found that two or more Al$_3$Ti particles could grow with their (001) planes perpendicular to one another from the same site.

In situ synchrotron X-ray radiography was employed to investigate the dynamics of Al$_{13}$Fe$_4$ formation on Al$_3$Ti. Fig. 5(a) shows an Al$_3$Ti crystal (highlighted by a yellow box) prior to the formation of any Al$_{13}$Fe$_4$ in the field of view (above the Al$_{13}$Fe$_4$ liquidus temperature). As cooling proceeded, Al$_{13}$Fe$_4$ started to develop (indicated by a yellow ellipse in Fig. 5(b)) on or from the pre-existing Al$_3$Ti. The subsequent frames show the growth of the newly formed Al$_{13}$Fe$_4$ crystals, and the yellow arrows indicate the dominant growth directions at different stages of growth.

At the earlier stages (Figs. 5(b) and (c)), the newly formed Al$_{13}$Fe$_4$ adopted a high-aspect-ratio, needle-like morphology and lengthened rapidly, with an average velocity of 21μm s^{-1} measured over the first 7 s of growth. Subsequently, the preferential lengthening slowed down, and instead lateral growth became dominant (along the yellow arrow in Fig. 5(d)), via which a large facet (with a final length > 400μm and width > 100μm) started to develop. The Al$_{13}$Fe$_4$ crystal progressively turned from a needle-like morphology to a plate-like morphology. The inset image in Fig. 5(e) provides a zoomed-in view of the advancing edge of the facet at time $t = 19$ s. Microscopic steps can be noticed, indicated by a red dashed line in the inset image of Fig. 5(e). Similar microscopic steps have been frequently observed in extracted Al$_{13}$Fe$_4$ [45], and other faceted IMCs such as Al$_{45}$Cr$_7$ [45], Al$_8$Mn$_5$ [58] and Cu$_6$Sn$_5$ [59], and were suggested to be associated with twin plane re-entrant grooves [45]. The large facets developed in this mechanism (Figs. 5(d) and (e)), and the crystal then thickened in the later stages (Fig. 5(f)), incorporating the Al$_3$Ti. Readers are invited to watch the radiographic video (Video 1) in the on-line SM, which gives a clearer impression of the growth dynamics and the role of microscopic steps.

In contrast to Fig. 5 that shows Al$_{13}$Fe$_4$ developing from a single Al$_3$Ti crystal, Fig. 6 shows an example of Al$_{13}$Fe$_4$ formation on pre-existing orthogonal Al$_3$Ti particles. Fig. 6(a) shows plate-like Al$_3$Ti crystals in an orthogonal arrangement, and the inset image shows

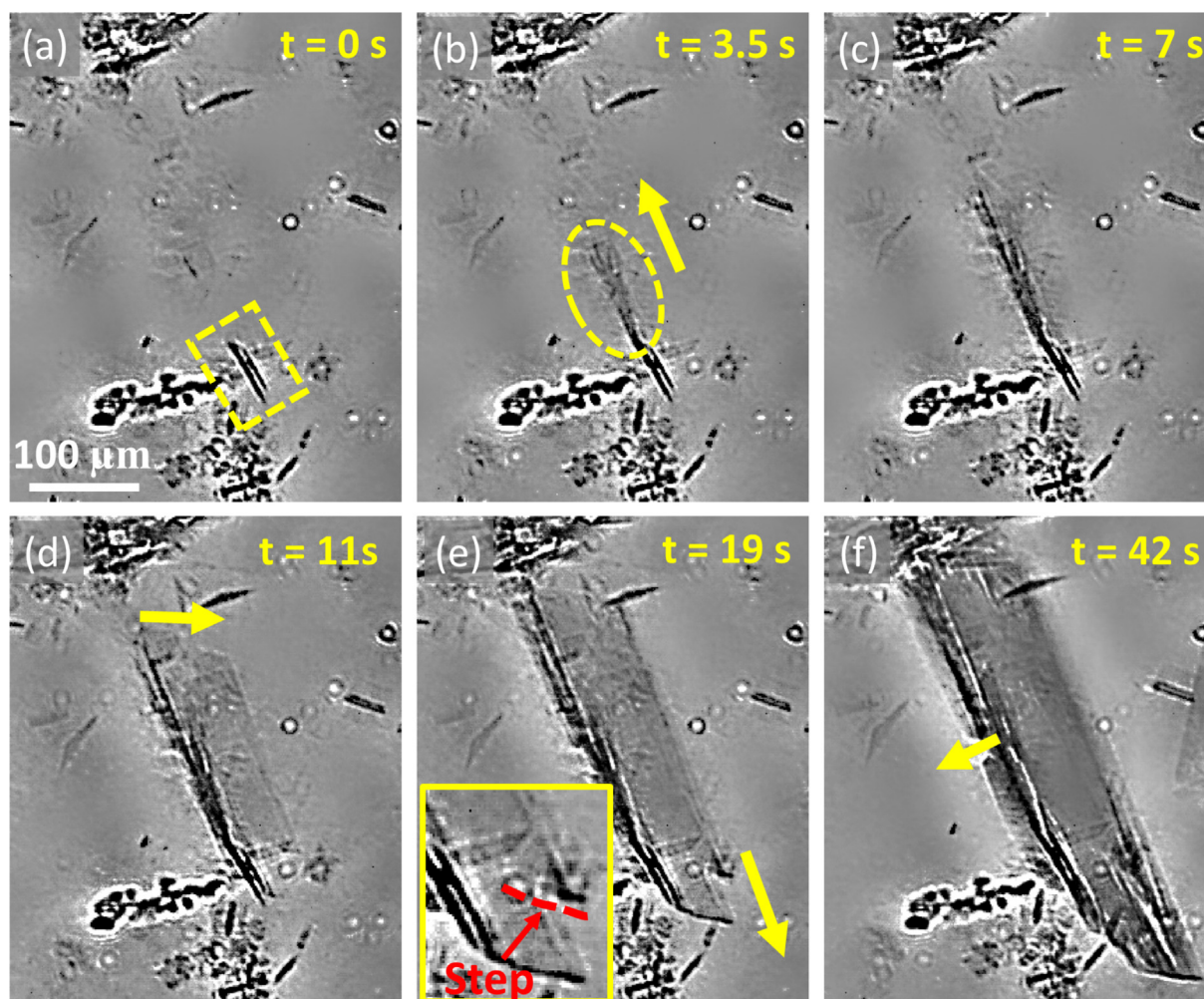**Fig. 5.** An X-ray radiograph sequence showing the development of an Al$_{13}$Fe$_4$ crystal from a pre-existing Al$_3$Ti crystal at 0.5K s^{-1}, under near-isothermal cooling. The yellow arrows indicate the dominant growth directions of the Al$_{13}$Fe$_4$ crystal at different stages of solidification.
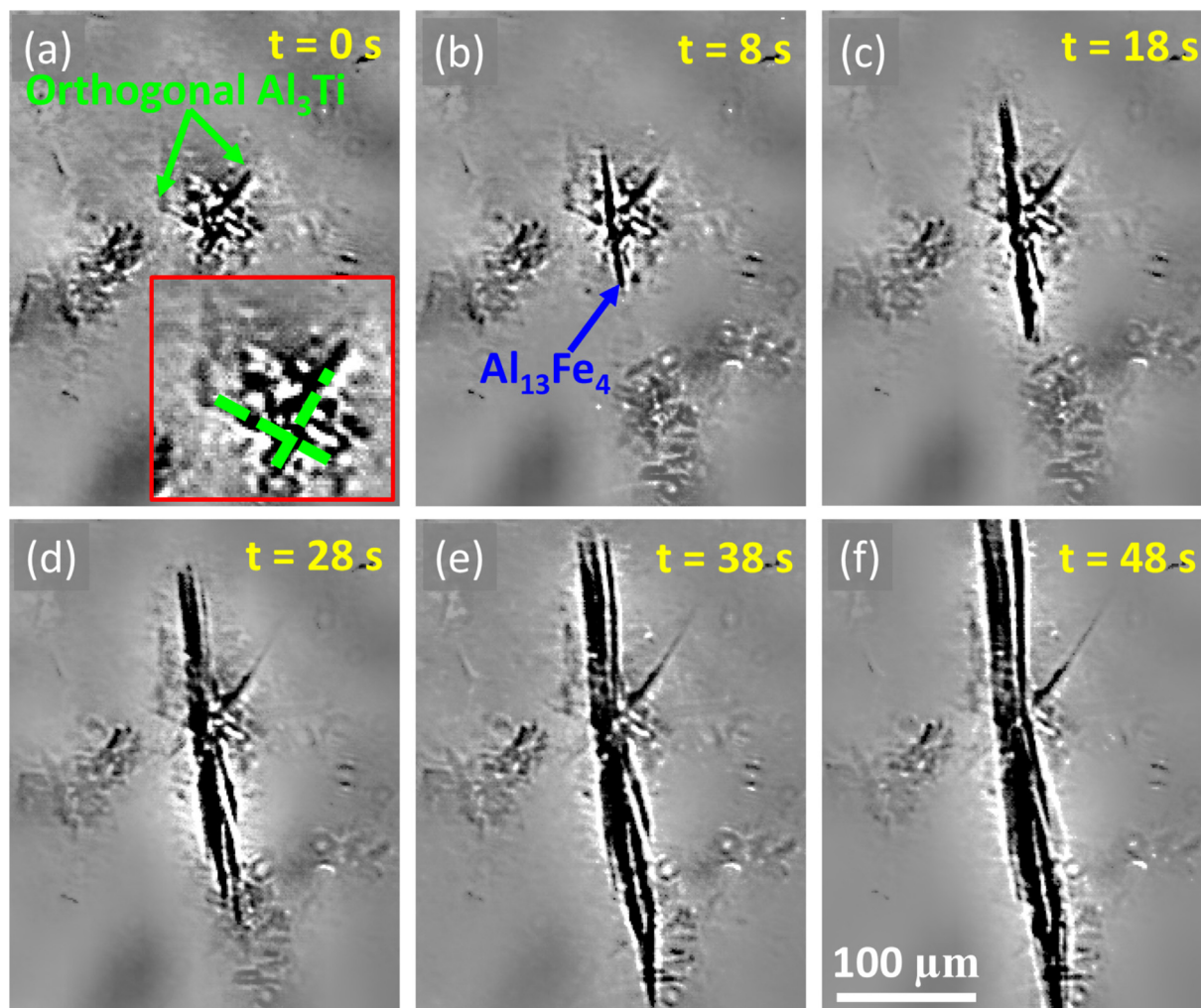
Fig. 6. An X-ray radiograph sequence showing the development of an $Al_{13}Fe_4$ crystal from pre-existing Al_3Ti crystals in an orthogonal configuration, at 0.25K s^{-1}, under near-isothermal cooling. The inset image in (a) provides a zoomed-in view of the Al_3Ti crystals, with green dashed lines superimposed to highlight the edges of the orthogonal Al_3Ti plates.

a zoomed-in view, with the superimposed green dashed lines highlighting the edges of the orthogonal Al_3Ti plates. Later, $Al_{13}Fe_4$ grew from the centre of the orthogonal Al_3Ti plates (Fig. 6(b)). The $Al_{13}Fe_4$ crystal in this case showed a similar growth behaviour to Fig. 5, with rapid lengthening at an earlier stage (Figs. 6(b) to (d)) and then thickening in the later stage of growth (Figs. 6(e) to (f)). Post-solidification EBSD maps and pole figures for these crystals in the solidified radiography sample are provided in Fig. S6 in the SM. The $Al_{13}Fe_4$ and Al_3Ti crystals possessed the same type of ORs as those in Figs. S5(a) to (d) under as-cast conditions.

Fig. S7 in the SM provides example radiographs that show IMCs in the Al-3Fe alloys without and with Ti additions. Correspondingly, Table S2 in the SM lists the average IMC size in these alloys.

X-ray CT was used to investigate the overall tendency of $Al_{13}Fe_4$ forming on Al_3Ti. Fig. 7(a) shows a 3-D volume rendering of Al-3Fe-0.7Ti in the as-cast condition, at magnification Mag 1 (4×), and Fig. 7(b) shows the Al_3Ti (green) and $Al_{13}Fe_4$ (blue) (with α-Al matrix removed) in the volume indicated by an orange box in Fig. 7(a), at magnification Mag 2 (20×). Fig. 7(c) is a zoomed-in view showing an $Al_{13}Fe_4$ plate associated with three orthogonal Al_3Ti plates.

Using these data, the tendency for $Al_{13}Fe_4$ to form on Al_3Ti was evaluated by studying the number of $Al_{13}Fe_4$ crystals with embedded Al_3Ti, facilitated by attenuation differences of the two phases.

286 $Al_{13}Fe_4$ crystals were identified in a sample volume of 10.4mm^3, out of which 151 (53%) had Al_3Ti embedded or partially embedded. This suggests that approximately 53% of the $Al_{13}Fe_4$ formed on Al_3Ti, likely an underestimate due to the resolution limit of the experiments. The formation of the other $Al_{13}Fe_4$ crystals might be associated with other inclusions, such as oxides or other particles too small to resolve. Similarly, *in situ* radiographic studies of an Al-3Fe (wt.%) alloy with Al-5Ti-1B (wt.%) additions suggested that ~50% of $Al_{13}Fe_4$ formed on Al_3Ti-containing inoculants [38].

4. Discussion

4.1. Orientation relationships between Al_3Ti and $Al_{13}Fe_4$

Following the method detailed in section S1.3 in the SM, 340 pairs of near-parallel, close-packed planes and 335 sets of full ORs were identified in 163 Al_3Ti - $Al_{13}Fe_4$ pairs by EBSD. As explained earlier, one Al_3Ti - $Al_{13}Fe_4$ pair can possess more than one OR because Al_3Ti was frequently embedded across twin domains of $Al_{13}Fe_4$. The colour map in Fig. 8(a) summarises the near-parallel, close-packed planes identified between Al_3Ti and $Al_{13}Fe_4$. {6̄23} and {620} were the mostly frequently involved planes for $Al_{13}Fe_4$, followed by {025}. The three plane families
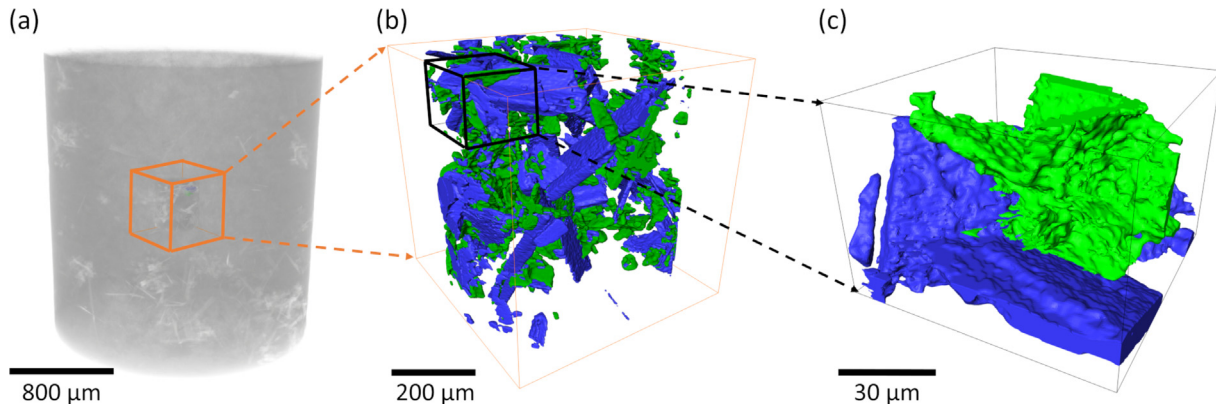
Fig. 7. (a) 3-D volume rendering of the Al-3Fe-0.7Ti sample in an as-cast condition, at magnification Mag 1. The orange box indicates the field of view of (b). (b) 3-D microstructure showing Al_3Ti (green) and $Al_{13}Fe_4$ (blue) at magnification Mag 2 (with α-Al matrix removed). (c) A zoomed-in view extracted from the black box in (b), showing an $Al_{13}Fe_4$ plate associated with orthogonal Al_3Ti plates.

had high similarity: d-spacings of 2.095Å for $\{\bar{6}23\}$, 2.101Å for $\{620\}$, and 2.048Å for $\{025\}$, and planar atomic densities of 16 atoms nm^{-2} for $\{\bar{6}23\}$, 18 atoms nm^{-2} for $\{620\}$, and 16 atoms nm^{-2} for $\{025\}$. Each of these plane families contained two symmetry-related planes (or four if including the parallel planes with a different sign) at approximately the same angle: 62.5° for $\{\bar{6}23\}$, 62.7° for $\{620\}$ and 60.9° for $\{025\}$.

The colour map in Fig. 8(b) summarises all the near-parallel, close-packed directions identified between Al_3Ti and $Al_{13}Fe_4$. $\langle001\rangle$ and $\langle102\rangle$ were the most frequently involved directions for $Al_{13}Fe_4$, in good correspondence with the two most prevalent near-parallel planes $\{620\}$ and $\{\bar{6}23\}$ in Fig. 8(a): $\langle001\rangle$ is the most close-packed direction on $\{620\}$, and $\langle102\rangle$ is the most close-packed direction on $\{\bar{6}23\}$.
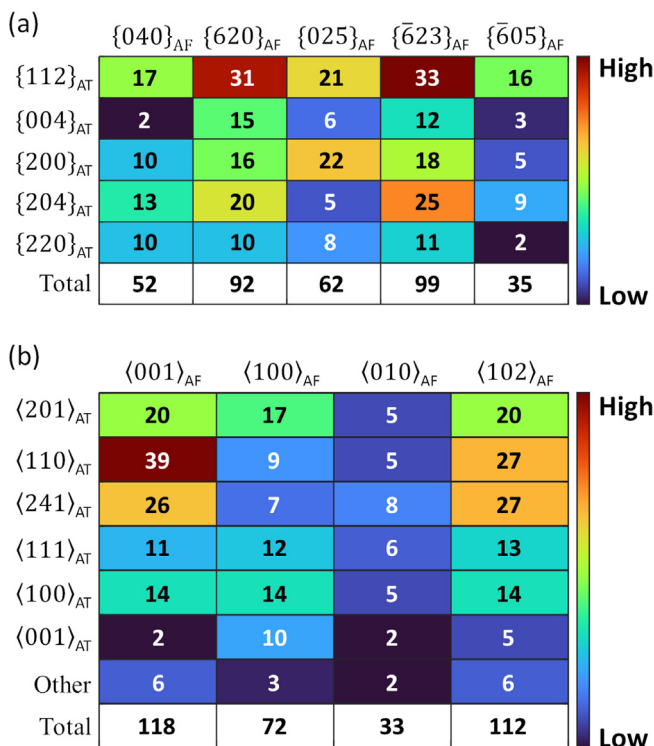
Taking into account of both the near-parallel planes and near-parallel directions, Table 4 lists the most frequent ORs between Al_3Ti and $Al_{13}Fe_4$. The bar chart in Fig. 9(a) shows the distribution of ORs, with their angular mismatch (calculated based on Euler angles according to section S1.3 in the SM) shown in Fig. 9(b). Overall, there was no predominant type of OR between Al_3Ti and $Al_{13}Fe_4$ (Fig. 9(a)). OR8 was the most frequently identified OR, and 16 out of 335 ORs (5%) fell into this type, where one of the $\{204\}$ planes in Al_3Ti was near-parallel with one of the $\{\bar{6}23\}$ planes in $Al_{13}Fe_4$ and one of the $\langle241\rangle$ directions in Al_3Ti was near-parallel with the $\langle102\rangle$ direction in $Al_{13}Fe_4$. The wide variety of ORs between Al_3Ti and $Al_{13}Fe_4$, corresponding to different types of interfaces, might account for the range of measured nucleation undercoolings of 10 to 30 K for $Al_{13}Fe_4$ [60]. The angular mismatch between the near-parallel planes and directions varied between 2° and 4° (Fig. 9(b)).

Table 4 and Fig. 9(a) show that the $\{112\}$ planes and $\langle110\rangle$ directions of Al_3Ti were frequently involved in the ORs: four out of eight ORs involved $\{112\}$ (OR1 to OR4) and $\langle110\rangle$ (OR1, OR3, OR5 and OR6), respectively. The $\{112\}$ planes and $\langle110\rangle$ directions of Al_3Ti were also frequently involved in the ORs when Al_3Ti catalysed α-Al nucleation [61,48,62]. For $Al_{13}Fe_4$, all the ORs were associated with either $\{620\}$ $\langle001\rangle$ or $\{\bar{6}23\}$ $\langle102\rangle$, and this is investigated in detail in Section 4.3.

4.2. Lattice misfit

An OR can be written in generic form $\{h'k'l'\}_N\langle u'v'w'\rangle_N // \{hkl\}_S\langle uvw\rangle_S$, where N denotes the nucleant, and S denotes the solid nucleus. $\langle u'v'w'\rangle$ and $\langle uvw\rangle$ are close-packed or nearly close-packed directions on the close packed

(a)

	$\{040\}_{AF}$	$\{620\}_{AF}$	$\{025\}_{AF}$	$\{\bar{6}23\}_{AF}$	$\{\bar{6}05\}_{AF}$	
$\{112\}_{AT}$	17	31	21	33	16	High
$\{004\}_{AT}$	2	15	6	12	3	
$\{200\}_{AT}$	10	16	22	18	5	
$\{204\}_{AT}$	13	20	5	25	9	
$\{220\}_{AT}$	10	10	8	11	2	
Total	52	92	62	99	35	Low

(b)

|	$\langle001\rangle_{AF}$	$\langle100\rangle_{AF}$	$\langle010\rangle_{AF}$	$\langle102\rangle_{AF}$	
$\langle201\rangle_{AT}$	20	17	5	20	High
$\langle110\rangle_{AT}$	39	9	5	27	
$\langle241\rangle_{AT}$	26	7	8	27	
$\langle111\rangle_{AT}$	11	12	6	13	
$\langle100\rangle_{AT}$	14	14	5	14	
$\langle001\rangle_{AT}$	2	10	2	5	
Other	6	3	2	6	
Total	118	72	33	112	Low

Fig. 8. Colour maps summarising (a) the near-parallel planes and (b) near-parallel directions identified between Al_3Ti and $Al_{13}Fe_4$. AT: Al_3Ti; AF: $Al_{13}Fe_4$.

Table 4
A list of the most frequent ORs between Al_3Ti and $Al_{13}Fe_4$. AT: Al_3Ti. AF: $Al_{13}Fe_4$.

	Parallel planes		Parallel directions	
	Al_3Ti	$Al_{13}Fe_4$	Al_3Ti	$Al_{13}Fe_4$
OR1	$\{112\}$	$\{620\}$	$\langle110\rangle$	$\langle001\rangle$
OR2	$\{112\}$	$\{620\}$	$\langle241\rangle$	$\langle001\rangle$
OR3	$\{112\}$	$\{\bar{6}23\}$	$\langle110\rangle$	$\langle102\rangle$
OR4	$\{112\}$	$\{\bar{6}23\}$	$\langle241\rangle$	$\langle102\rangle$
OR5	$\{004\}$	$\{620\}$	$\langle110\rangle$	$\langle001\rangle$
OR6	$\{004\}$	$\{\bar{6}23\}$	$\langle110\rangle$	$\langle102\rangle$
OR7	$\{204\}$	$\{620\}$	$\langle241\rangle$	$\langle001\rangle$
OR8	$\{204\}$	$\{\bar{6}23\}$	$\langle241\rangle$	$\langle102\rangle$

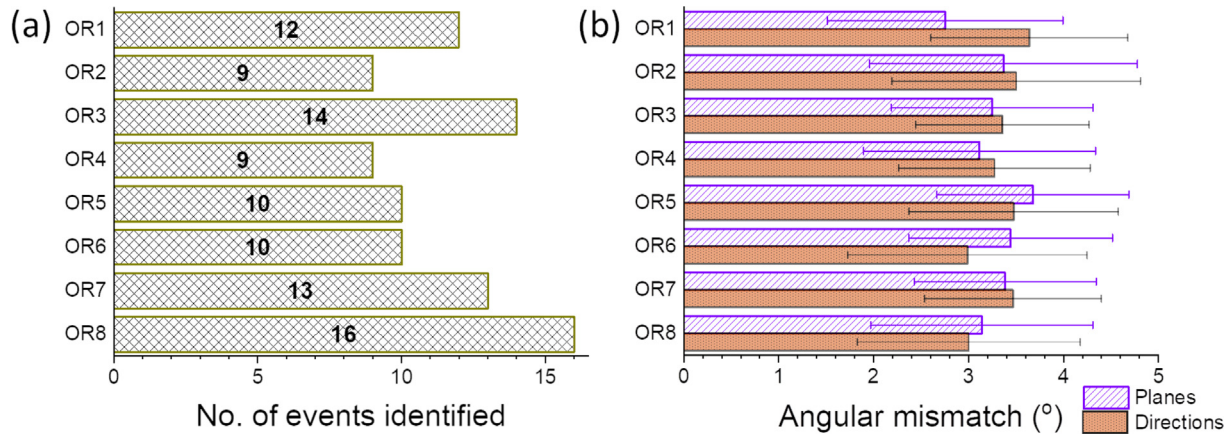**Fig. 9.** (a) A bar chart showing the distribution of the most frequent ORs between Al$_3$Ti and Al$_{13}$Fe$_4$. The corresponding planes and direction of the ORs are provided in Table 4. (b) A bar chart showing the angular mismatch of the corresponding planes and direc.tion of each OR.

planes $\{h'k'l'\}$ and $\{hkl\}$, respectively. The lattice misfit at the solid nucleus/nucleant interface is defined as [50]:

$$f = \frac{|r_{\langle uvw \rangle} - r_{\langle u'v'w' \rangle}|}{r_{\langle uvw \rangle}} \qquad (4)$$

where $r_{\langle uvw \rangle}$ and $r_{\langle u'v'w' \rangle}$ are the interatomic distances along the close-packed directions $\langle uvw \rangle$ (of the nucleus) and $\langle u'v'w' \rangle$ (of the nucleant), respectively.

Fig. 10(a) shows the lattice misfit f associated with the ORs in Table 4 and Fig. 9. A list of $r_{\langle uvw \rangle}$ and $r_{\langle u'v'w' \rangle}$ used for the lattice misfit calculation is provided in Table S3 in the SM. The misfits all fell below 10% (Fig. 10(a)), commonly accepted as a low misfit strain in models of this type [63,50,48,64].

For lattice misfits <10%, the epitaxy theory, first proposed by Frank and Van der Merwe [65], links misfit, misfit strain energy and interface formation. More recently the theory was adopted by Fan et al. in an epitaxial nucleation model [50] that concerned early-stage nucleation in particular.

In the epitaxy model, heterogeneous nucleation, at an undercooling beyond a critical undercooling, is assumed to occur epitaxially via atom-by-atom building of the new solid phase on the nucleant "template". The initial structure of the solid nucleus is

pseudomorphic, mimicking the crystal structure of the substrate. Elastic strain energy increases as the pseudomorphic solid layer builds up, due to the lattice misfit between the solid and the substrate (f in Eq. 4). The elastic strain energy per unit area E_S is related to f and the pseudomorphic layer thickness h via [50]:

$$E_S = \frac{2\mu(1+v)}{1-v}f^2 h \qquad (5)$$

where μ is the shear modulus of the nucleus material, and v is the Poisson's ratio. This elastic strain energy can be accommodated in the pseudomorphic structure via lattice distortion up to a critical layer thickness h_c, above which the stored strain energy destabilises the arrangement [50]. Nucleation can only continue if the strain energy is relieved or accommodated by strain relaxation such as the formation of dislocations and stacking faults. Assuming strain relaxation only via misfit dislocations [66,50,67], the dislocation energy per unit area E_D can be written as:

$$E_D = \frac{\mu}{2\pi(1-v)}fb\left(ln\frac{h_c}{b}+1\right) \qquad (6)$$

where b is the Burger's vector. For Al$_{13}$Fe$_4$, the magnitude of the Burger's vector is 0.8 nm [68]. The critical thickness h_c is defined
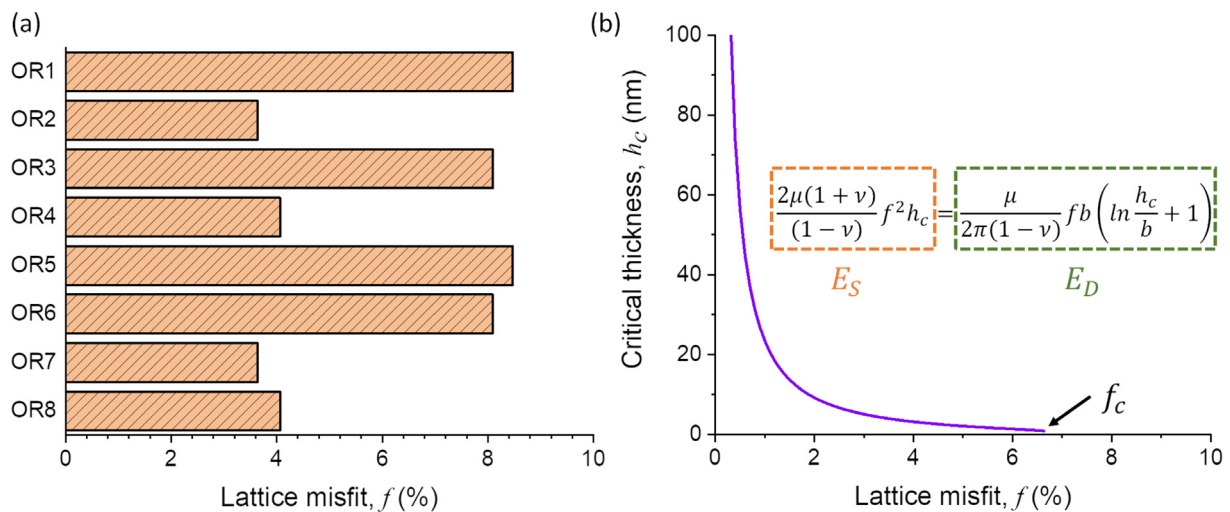

Fig. 10. (a) A bar chart of the lattice misfit f associated with the ORs in Table 4 and Fig. 9. (b) The critical layer thickness h_c as a function of the lattice misfit f for Al$_{13}$Fe$_4$, calculated from Eq. 7 based on the epitaxial nucleation model. E_S is the elastic strain energy per unit area, E_D is the dislocation energy per unit area, μ is the shear modulus, v is the Poisson's ratio, and b is the Burger's vector of Al$_{13}$Fe$_4$. Parameters used for calculation are: $b = 0.8$ nm and $v = 0.2$.

as the layer thickness at which the strain energy equals the dislocation energy, assuming complete strain relaxation [50,67]:

$$\frac{2\mu(1+\nu)}{1-\nu}f^2 h_c = \frac{\mu}{2\pi(1-\nu)}fb(ln\frac{h_c}{b}+1)$$
$$h_c = \frac{b}{4\pi(1+\nu)f}(ln\frac{h_c}{b}+1) \qquad (7)$$

Noting that h_c is on both sides of Eq. 7 and so solving numerically, Fig. 10(b) shows that h_c decreases rapidly with increasing f. A critical misfit f_c can also be assumed of $h_c = b$, beyond which lattice misfit cannot be accommodated by misfit dislocations. Under these conditions, the critical misfit for $Al_{13}Fe_4$ was $f_c \approx 6.7\%$ (Fig. 10(b)), which agrees well with the lattice misfit of the experimentally identified ORs (Fig. 10(a)). In practice, mechanisms in addition to misfit dislocations may also accommodate misfit strain, such as stacking faults. This may be supported by the finding that twinning was identified in all the $Al_{13}Fe_4$ crystals.

Noting that the $Al_{13}Fe_4$ forms on Al_3Ti at 710° C, the temperature dependence of the lattice misfit should also be assessed. Therefore, lattice parameters for the phases were obtained from refined synchrotron X-ray diffraction data taken at 25° C to 500° C. The results are available as Fig. S8 in the SM. Although both the $Al_{13}Fe_4$ and Al_3Ti latices expanded as the temperature increased, the resultant changes in the lattice parameters were negligible compared with the misfit between the two lattices. The lattice misfit therefore remained largely insensitive (variation < 0.1%) to temperature in this temperature range. Although data was not available at 710° C, given the melting points of $Al_{13}Fe_4$ (1160° C) and Al_3Ti (1412° C), it is reasonable to assume that lattice misfit was relatively insensitive to temperature under the temperature range studied.

4.3. Twinning

Twinning was identified in all $Al_{13}Fe_4$ particles, and Al_3Ti particles were preferentially sited on (such as Fig. 1(h) and and Al_3Ti particle 2 in Fig. 4(c)) or across $Al_{13}Fe_4$ twin boundaries (such as Al_3Ti particle 1 and 3 in Fig. 4(c)). Because of this, an Al_3Ti crystal could possess multiple ORs with the different $Al_{13}Fe_4$ twin domains. Among 163 Al_3Ti - $Al_{13}Fe_4$ pairs, 56 (34%) possessed 2 ORs and 51 (31%) possessed 3 or more ORs.

The FSE image in Fig. 11(a), together with the Euler angle map (Fig. 11(b)) and phase map (Fig. 11(c)), shows an Al_3Ti crystal sitting across multiple twin domains in an $Al_{13}Fe_4$ crystal (labelled "A" to "G" in Fig. 11(b)). Two types of twinning were identified: {100} twins and {001} twins. {100} twins included A (purple area) and B (light blue area), C (brown area) and D (grey area), and E (green area) and G (red area). {001} twins included A (purple area) and C (brown area), E (green area) and F (blue area), and D (grey area) and G (red area). Pole figures for the twin planes and common direction are provided in Fig. S9 in the SM. Fig. 11(d) shows the unit cells for {100} twins (i.e. sharing a {100} interface) and {001} twins (i.e. sharing a {001} interface), viewed along the common ⟨010⟩ direction. The same types of twins were reported by EBSD studies on primary $Al_{13}Fe_4$ solidified at cooling rates up to 5 Ks⁻¹ [8,45], and by selected area electron diffraction (SAED) on eutectic $Al_{13}Fe_4$ solidified at cooling rates up to ~1 Ks⁻¹ [69]. However differently from previous work that focused on the identification of $Al_{13}Fe_4$ twinning, here we investigate the relationship with the Al_3Ti nucleant.

The pole figures in Fig. 11(e) show the ORs between the Al_3Ti and different twin domains of the $Al_{13}Fe_4$ crystal, which are also illustrated by unit cell wire frames in Fig. 11(f). Domains A, B, C, E and F of the $Al_{13}Fe_4$ had close packed planes and directions near-parallel with the same {200} plane and ⟨201⟩ direction of the Al_3Ti, whereas D did not. The near-parallel planes and directions are marked by red and orange circles respectively in the pole

figures, and also highlighted in the unit cell wire frames. Because A and B were {100} twins, identified as a 180° rotation about the common ⟨001⟩ axis [8], their {620} planes (and other planes containing the common ⟨001⟩ axis) remained parallel. Likewise, for the {001} twinning E and F, identified as a 180° rotation about the common ⟨100⟩ axis [8], the {025} planes (and other planes containing the common ⟨100⟩ axis) also remained parallel.

Similarly, the {620} ⟨001⟩ of a parent crystal in $Al_{13}Fe_4$ was parallel to the {$\bar{6}$23} ⟨102⟩ of its {001} twin, such as A and C. This is consistent with earlier investigations by SAED that revealed that the {620} diffraction spots along [001] overlapped with the {$\bar{6}$23} spots along [102] for $Al_{13}Fe_4$, which also contained {001} twins [70]. This {001} twinning led to a pseudo-orthorhombic symmetry, as proposed earlier by Ma et al., and is indicated by the yellow dashed frame in Fig. 11(d). The lattice parameters a_o, b_o and c_o of the pseudo-orthorhombic cell had the following relationships with the lattice parameters a, b and c of the original monoclinic cell [70]: $a_o = a/2, b_o = b/2, c_o = 2c\cos(\beta - 90°)$, where β is the angle between the a and c axis in the monoclinic cell.

To explore the pseudo-orthorhombic symmetry further, the $Al_{13}Fe_4$ crystal in Fig. 11(a) was re-indexed using the pseudo-orthorhombic cell described above, and is shown in Fig. 11(g). Comparing Fig. 11(g) with Fig. 11(b) shows that all the {001} twins disappear, as they are now contained in the pseudo-orthorhombic cell. The two twin domains in Fig. 11(g), identified as {101} twinning (with details provided in Fig. S10 in the SM), had the identical OR with the Al_3Ti (as shown in Fig. 11(h)):

$$\{200\}_{AT}//\{313\}_{AF_o}; \langle 201\rangle_{AT}//\langle 101\rangle_{AF_o} \qquad (8)$$

where AF_o denotes $Al_{13}Fe_4$ indexed using a pseudo-orthorhombic cell. {313} is the most close-packed plane and ⟨101⟩ is the most close-packed direction of pseudo-orthorhombic $Al_{13}Fe_4$ [71].

Using the same approach, the {620} ⟨001⟩ and {$\bar{6}$23} ⟨102⟩ planes and directions of $Al_{13}Fe_4$ in the ORs in Table 4 can be unified to {313} ⟨101⟩, and the eight ORs in Table 4 merged into four:

$$OR1^*: \{112\}_{AT}//\{313\}_{AF_o}; \langle 110\rangle_{AT}//\langle 101\rangle_{AF_o} \qquad (9)$$

$$OR2^*: \{112\}_{AT}//\{313\}_{AF_o}; \langle 241\rangle_{AT}//\langle 101\rangle_{AF_o} \qquad (10)$$

$$OR3^*: \{004\}_{AT}//\{313\}_{AF_o}; \langle 110\rangle_{AT}//\langle 101\rangle_{AF_o} \qquad (11)$$

$$OR4^*: \{204\}_{AT}//\{313\}_{AF_o}; \langle 241\rangle_{AT}//\langle 101\rangle_{AF_o} \qquad (12)$$

The frequently observed interfaces/ORs between Al_3Ti and multiple $Al_{13}Fe_4$ twin domains, combined with the insights of epitaxial nucleation model in Section 4.2, suggest that twinning likely developed almost immediately after the formation of few-layer $Al_{13}Fe_4$, to accommodate partially the misfit strain between $Al_{13}Fe_4$ and Al_3Ti. All the subsequent ORs then related to the pseudo-orthorhombic symmetry of $Al_{13}Fe_4$; twinning-related pseudo-symmetry has also been reported in other Fe-rich IMCs, such as β-AlFeSi [72]. In general terms, the findings suggest that an efficient nuclant for $Al_{13}Fe_4$ should have a misfit < 6.7% with the {313} ⟨101⟩ of the pseudo-orthorhombic $Al_{13}Fe_4$ (Fig. 10(b)), as is the case here for Al_3Ti.

4.4. Wider applicability

To assess if the applicability of the key finding, i.e. the twinning-related formation of $Al_{13}Fe_4$ on inoculant particles, could be extended to more commercially relevant alloys to control IMC formation, as hypothesised in the introduction, 0.5 wt. % Ti was added to a commercial 6xxx alloy. Note the alloy had no pre-existing grain refining Al-5Ti-1B master alloy or other added inoculants. Further, to simulate a Fe-contaminated recy-
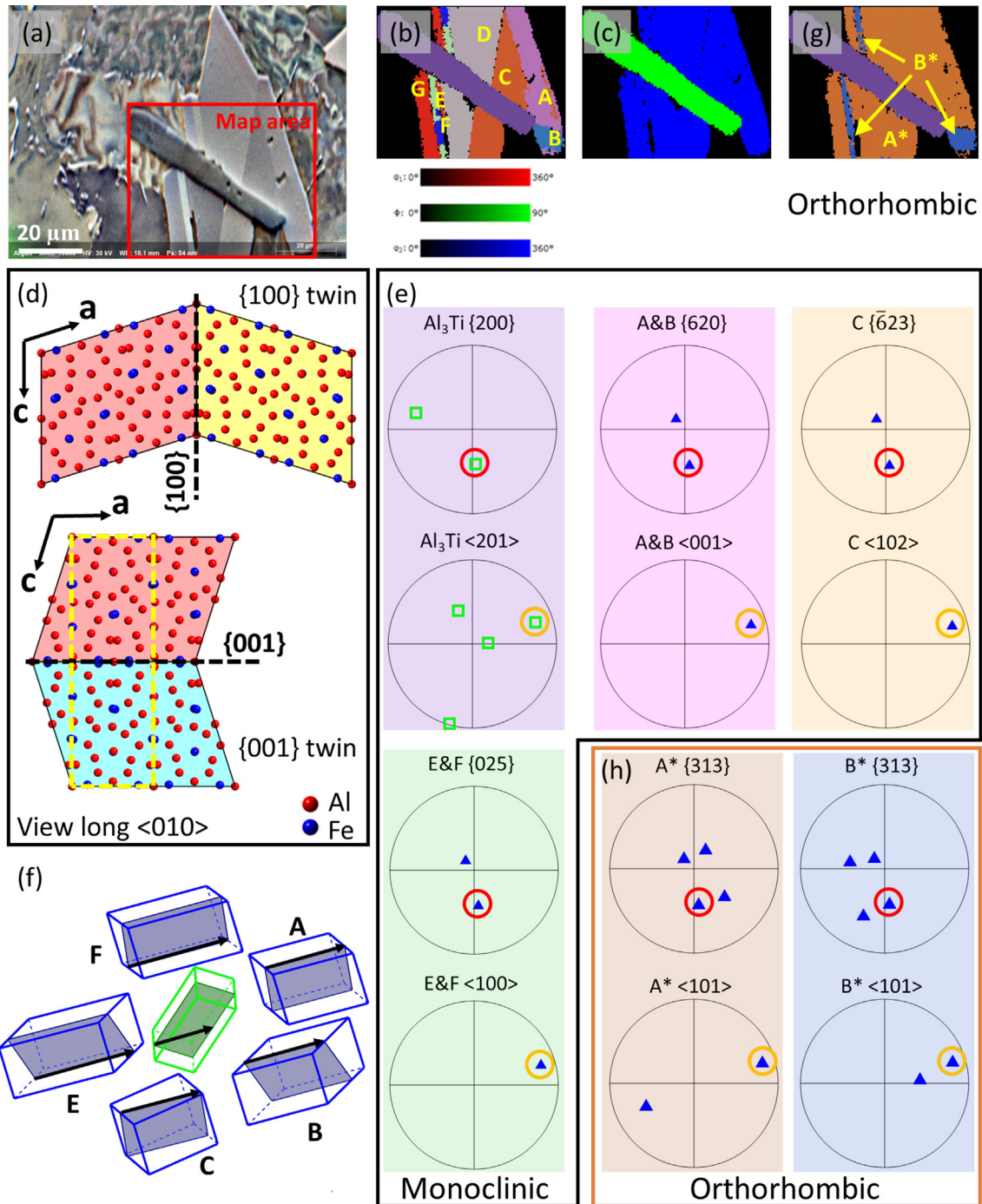
Fig. 11. (a) An FSE image showing Al₃Ti embedded in an Al₁₃Fe₄ crystal. The red box indicates the area of EBSD maps. (b) An EBSD Euler angle map revealing that the Al₃Ti sat across multiple twins of the Al₁₃Fe₄ (denoted as "A" to "G"). (c) An EBSD phase map showing the Al₁₃Fe₄ and the Al₃Ti. (d) Unit cells of {100} twins and {001} twins, viewed along the common ⟨010⟩ direction. The yellow dashed frame indicates a pseudo-orthorhombic unit cell arising from {001} twinning. (e) Pole figures showing the ORs identified between the Al₃Ti and different twin domains of the Al₁₃Fe₄. The near-parallel planes are marked by red circles and the near-parallel directions are marked by orange circles. (f) Unit cell wire frames illustrating the ORs identified in (e), with the near-parallel planes and directions highlighted. (g) An EBSD Euler angle map of the same crystals when the Al₁₃Fe₄ was indexed with its pseudo-orthorhombic unit cell. (h) Corresponding pole figures showing the ORs between the Al₃Ti and the Al₁₃Fe₄ indexed with its pseudo-orthorhombic unit cell.

cled alloy, it had a relatively high, hyper-eutectic Fe concentration of 2.2 wt.%. As with the model Al-Fe-Ti alloy, the hypothesis was to first form Al₃Ti as a population of effective inoculants for the subsequent formation of Al₁₃Fe₄. The alloy composition is listed in Table S4 in the SM, and a description of the equilibrium solidification sequence of this alloy is provided in Fig. S11 in the SM.

The alloy was solidified at cooling rates ranging from 0.5 K to 4 K s⁻¹, and Figs. 12(a) and (b) show FSE images of Al₃Ti sitting at the twin boundaries of Al₁₃Fe₄ at 0.5 K s⁻¹ and 4 K s⁻¹ respectively, identical to the Al-Fe-Ti model alloy, suggesting wider applicability of the earlier findings to commercial Al alloys.

In a 6xxx series alloy with relatively low Fe concentration, α-Al forms first as the primary phase and Fe-rich IMCs form as sec-

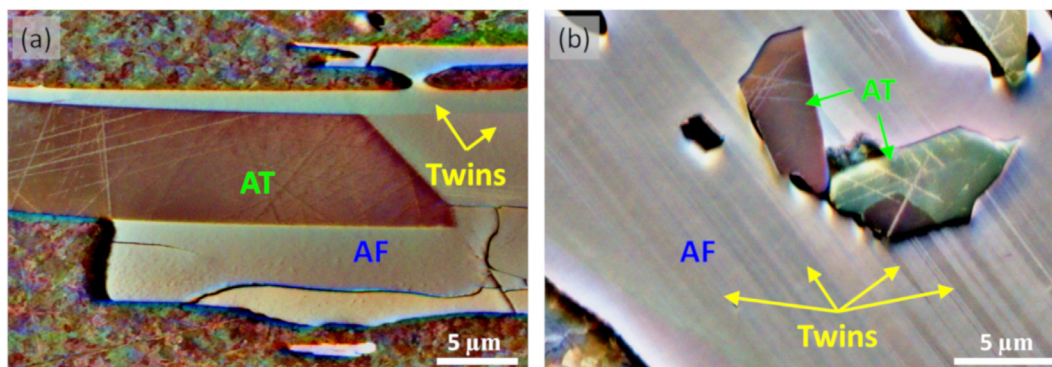**Fig. 12.** FSE images of Al$_3$Ti associated with Al$_{13}$Fe$_4$ twins in a 6xxx + Fe + Ti alloy, at cooling rates of (a) 0.5K s^{-1} and (b) 4K s^{-1}.

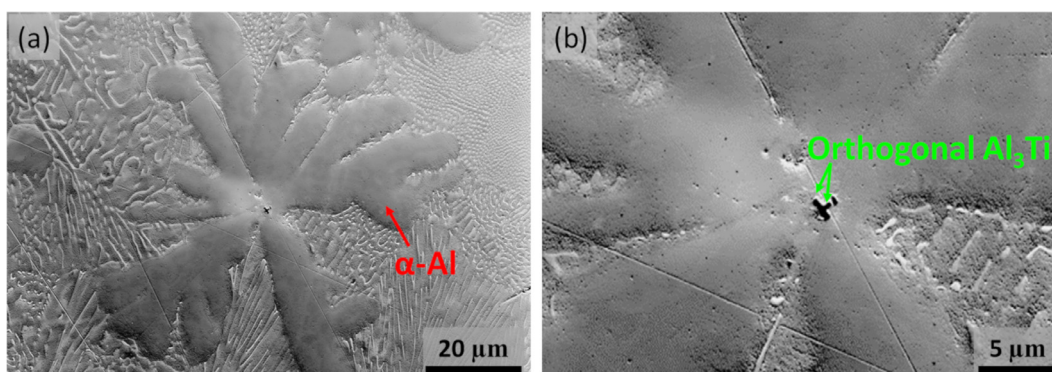**Fig. 13.** (a) A secondary electron image of an equiaxed Al dendrite (formed as a divorced eutectic following the primary Al$_{13}$Fe$_4$) in the 6xxx + Fe + Ti alloy at 4K s^{-1}. (b) A secondary electron image at a higher magnification, revealing orthogonal Al$_3$Ti plates (of ∼1μm) located in the centre of the dendrite.

ondary phases. The α-Al will nucleate on the relatively large, more potent Al$_3$Ti (or Al$_3$Ti-coated TiB$_2$) inoculant particles at a small undercooling < 1 K. [73,27]. Although the subsequent Fe-rich IMCs can form on any remaining, less efficient (smaller) nucleants [31], because the ordered IMCs have a relatively high nucleation barrier, this is comparatively difficult and the refining effect weak [74]. Instead, growth of a small number of very large IMCs tends to dominate. In contrast, in the 6xxx + Fe + Ti alloy of hyper-eutectic Fe concentration, it was now the Fe-rich IMCs that formed first (not α-Al) on the larger, more potent Al$_3$Ti particles (such as those in Fig. 12). As cooling continued, α-Al subsequently formed but now via eutectic reaction, as shown by the equilibrium solidification sequence in Fig. S11 in the SM. The α-Al formed as a divorced eutectic, for example as shown in Fig. 13(a) with a large equiaxed dendrite surrounded by α-Al/IMC eutectic colonies. Intriguingly, the higher magnification view in Fig. 13(b) shows orthogonal Al$_3$Ti plates in the dendrite centre. The Al$_3$Ti plate was smaller (∼1μm) than that typically embedded in primary Al$_{13}$Fe$_4$ (∼5μm).

Thus we conclude that while some larger Al$_3$Ti nucleated the primary Fe-rich IMC (Fig. 12), unlike the case of where α-Al is nucleated first, there were sufficient *effective* Al$_3$Ti nucleants left to nucleate α-Al in the eutectic reaction (Fig. 13). This arises because α-Al is comparatively easy to nucleate and does not rely on the most efficient nucleants being available [75]. It can be speculated further that because the more efficient nucleants for α-Al were removed by the prior IMC formation, the less efficient nucleants remaining resulted in a slightly higher nucleation undercooling for α-Al: 0.6 K for α-Al to nucleate on a relatively small, 1 μm Al$_3$Ti particle, compared with 0.1 K on a relatively large, 5 μm Al$_3$-Ti particle according to the free growth model [73]. Higher undercoolings promote the tendency for burst nucleation of α-Al that can

result in finer dendrites [32,76,75]. Further work will investigate this approach quantitatively and whether it has the potential to refine *both* primary IMCs and α-Al in recycled alloys of significantly elevated Fe concentration.

5. Conclusions

As a possible route to gaining greater influence over Fe-rich IMC formation in recycled Al alloys, Ti was added to high Fe-containing Al alloys to produce a large number of Al$_3$Ti particles, a potentially efficient inoculant for Al$_{13}$Fe$_4$. The formation and growth of Al$_{13}$Fe$_4$ on pre-existing Al$_3$Ti were studied systematically combining EBSD, *in situ* synchrotron X-ray radiography and laboratory-based X-ray CT, first in a model Al-Fe alloy, and then with key insights confirmed in a recycled commercial 6xxx alloy. The key insights were:

1. Al$_3$Ti particles frequently had an orthogonal configuration, and the Al$_{13}$Fe$_4$ was associated preferentially with these Al$_3$Ti particles: EBSD revealed that up to 49% of the Al$_{13}$Fe$_4$ crystals in the model alloy contained two or more Al$_3$Ti plates with the orthogonal morphology.
2. Direct evidence of Al$_{13}$Fe$_4$ forming on Al$_3$Ti was provided by it *in situ* X-ray radiography. The Al$_{13}$Fe$_4$ first developed from Al$_3$Ti with a needle-like morphology by rapid unidirectional growth, which was followed by the development of the crystal facets via lateral growth, and then crystal thickening in the later stage of solidification.
3. X-ray CT analysis on the model alloy showed that approximately 53% of the Al$_{13}$Fe$_4$ crystals contained Al$_3$Ti, suggesting that their formation was associated with Al$_3$Ti. This was likely an underestimate due to the resolution limit of the experi-

ments. The proportion was consistent with earlier findings when Al-5Ti-1B was added to the same model Al-Fe alloy, where ~50% $Al_{13}Fe_4$ crystals were estimated to form on Al_3Ti-containing inoculants.

4. The lattice misfit of the experimentally identified ORs between $Al_{13}Fe_4$ and Al_3Ti showed good agreement with a critical misfit of 6.7% predicted based on an epitaxial nucleation model, supporting an epitaxial nucleation mechanism for the formation of $Al_{13}Fe_4$ on Al_3Ti.

5. Microscopic twins were identified in all $Al_{13}Fe_4$ crystals, and the formation of $Al_{13}Fe_4$ on Al_3Ti was strongly linked with twinning. This behaviour was also verified in a recycled 6xxx alloy. Twinning was suggested to start early during the formation of $Al_{13}Fe_4$ on Al_3Ti.

6. The {001} twinning of $Al_{13}Fe_4$ gave rise to a pseudo-orthorhombic symmetry. Re-indexing the $Al_{13}Fe_4$ with the pseudo-orthorhombic cell showed that ORs between $Al_{13}Fe_4$ and Al_3Ti were preferentially associated with the most close-packed plane and direction of the pseudo-orthorhombic $Al_{13}Fe_4$.

7. When exploring new, more potent nucleants for $Al_{13}Fe_4$ and other crystallographically closely related IMCs such as β-AlFeSi, it is important to consider the pseudo-symmetry of the IMCs. Potent nucleants should have minimal misfit with the most close-packed planes and directions of the pseudo-symmetry cell of the IMCs, which can be used as a guideline for fast screening of efficient nucleants for low-symmetry IMCs.

Data availability

Data will be made available on request.

Declaration of Competing Interest

The authors declare that they have no known competing financial interests or personal relationships that could have appeared to influence the work reported in this paper.

Acknowledgements

Appendix A. Supplementary data

Supplementary data associated with this article can be found, in the online version, at https://doi.org/10.1016/j.matdes.2023.112110.

References

[1] D. Raabe, D. Ponge, P.J. Uggowitzer, M. Roscher, M. Paolantonio, C. Liu, H. Antrekowitsch, E. Kozeschnik, D. Seidmann, B. Gault, F. De Geuser, A. Deschamps, C. Hutchinson, C. Liu, Z. Li, P. Prangnell, J. Robson, P. Shanthraj, S. Vakili, C. Sinclair, L. Bourgeois, S. Pogatscher, Making sustainable aluminum by recycling scrap: The science of "dirty alloys", Prog. Mater. Sci. 128 (2022) 100947.

[2] J.A. Taylor, Iron-Containing Intermetallic Phases in Al-Si Based Casting Alloys, Procedia Mater. Sci. 1 (2012) 19–33.

[3] S. Ji, W. Yang, F. Gao, D. Watson, Z. Fan, Effect of iron on the microstructure and mechanical property of Al–Mg–Si–Mn and Al–Mg–Si diecast alloys, Mater. Sci. Eng. A 564 (2013) 130–139.

[4] Z. Jin, C. Cai, T. Hashimoto, Y. Yuan, D.H. Kang, J. Hunter, X. Zhou, The behaviour of iron-containing intermetallic particles in aluminium alloys in alkaline solution, Corros. Sci. 179 (2021) 109134.

[5] A. Bjurenstedt, D. Casari, S. Seifeddine, R.H. Mathiesen, A.K. Dahle, In-situ study of morphology and growth of primary α-Al(FeMnCr)Si intermetallics in an Al-Si alloy, Acta Mater. 130 (2017) 1–9.

[6] S. Feng, E. Liotti, A. Lui, S. Kumar, A. Mahadevegowda, K.A.Q. O'Reilly, P.S. Grant, An in-situ method to estimate the tip temperature and phase selection of secondary Fe-rich intermetallics using synchrotron X-ray radiography, Scr. Mater. 149 (2018) 44–48.

[7] B. Cai, A. Kao, P. Lee, E. Boller, H. Basevi, A. Phillion, A. Leonardis, K. Pericieous, Growth of β intermetallic in an Al-Cu-Si alloy during directional solidification via machine learned 4D quantification, Scr. Mater. 165 (2019) 29–33.

[8] S. Feng, Y. Cui, E. Liotti, A. Lui, C. Gourlay, P. Grant, In-situ X-ray radiography of twinned crystal growth of primary Al13Fe4, Scr. Mater. 184 (2020) 57–62.

[9] Y. Zhao, W. Zhang, D. Song, B. Lin, F. Shen, D. Zheng, C.X. Xie, Z. Sun, Y. Fu, R. Li, Nucleation and growth of Fe-rich phases in Al-5Ti-1B modified Al-Fe alloys investigated using synchrotron X-ray imaging and electron microscopy, J. Mater. Sci. Technol. 80 (2021) 84–99.

[10] Z. Song, O.V. Magdysyuk, L. Tang, T. Sparks, B. Cai, Growth dynamics of faceted Al13Fe4 intermetallic revealed by high-speed synchrotron X-ray quantification, J. Alloys Compd. 861 (2021) 158604.

[11] S. Feng, E. Liotti, P.S. Grant, X-ray Imaging of Alloy Solidification: Crystal Formation, Growth, Instability and Defects, Materials (Basel) 15 (4) (2022) 1319.

[12] Y. Zhao, D. Song, H. Wang, X. Li, L. Chen, Z. Sun, Z. Wang, T. Zhai, Y. Fu, Y. Wang, S. Liu, Y. Du, W. Zhang, Revealing the nucleation and growth mechanisms of Fe-rich phases in Al–Cu–Fe(-Si) alloys under the influence of Al–Ti–B, Intermetallics 146 (2022) 107584.

[13] S. Feng, I. Han, A. Lui, R. Vincent, G. Ring, P.S. Grant, E. Liotti, Investigating Metal Solidification with X-ray Imaging, Metals (Basel) 12 (3) (2022) 395.

[14] H.W.L. Phillips, Equilibrium diagrams of aluminium alloy systems, Aluminium Development Association, London, 1961.

[15] K. Liu, X. Cao, X. Chen, Precipitation of iron-rich intermetallic phases in Al-4.6Cu-0.5Fe-0.5Mn cast alloy, J. Mater. Sci. 47 (10) (2012) 4290–4298.

[16] Z. Que, C. Fang, C.L. Mendis, Y. Wang, Z. Fan, Effects of Si solution in θ-Al13Fe4 on phase transformation between Fe-containing intermetallic compounds in Al alloys, J. Alloys Compd. 932 (2023) 167587.

[17] G. Sha, K.A.Q. O'Reilly, B. Cantor, J.M. Titchmarsh, R. Hamerton, Quasi-peritectic solidification reactions in 6xxx series wrought Al alloys, Acta Mater. 51 (7) (2003) 1883–1897.

[18] A. Verma, S. Kumar, P. Grant, K. O'Reilly, Influence of cooling rate on the Fe intermetallic formation in an AA6063 Al alloy, J. Alloys Compd. 555 (2013) 274–282.

[19] Z. Que, C.L. Mendis, Formation of θ-Al13Fe4 and the multi-step phase transformations to α-Al8Fe2Si, β-Al5FeSi and δ-Al4FeSi2 in Al–20Si-0.7Fe alloy, Intermetallics 127 (2020) 106960.

[20] L. Zhang, J. Gao, L.N.W. Damoah, D.G. Robertson, Removal of Iron From Aluminum: A Review, Miner. Process. Extr. Metall. Rev. 33 (2) (2012) 99–157.

[21] H. Becker, T. Bergh, P.E. Vullum, A. Leineweber, Y. Li, Effect of Mn and cooling rates on α-, β- and δ-Al–Fe–Si intermetallic phase formation in a secondary Al–Si alloy, Materialia 5 (2019) 100198.

[22] E. Cinkilic, C.D. Ridgeway, X. Yan, A.A. Luo, A Formation Map of Iron-Containing Intermetallic Phases in Recycled Cast Aluminum Alloys, Metall. Mater. Trans. A Phys. Metall. Mater. Sci. 50 (12) (2019) 5945–5956.

[23] M. Sha, S. Wu, X. Wang, L. Wan, Effects of Co addition on Fe-bearing intermetallic compounds and mechanical properties of AlSi20Cu2Ni1Fe0.7–1 alloys, J. Alloys Compd. 551 (2013) 468–474.

[24] N. Nordin, S. Farahany, T. Abu-Bakar, E. Hamzah, A. Ourdjini, Microstructure development, phase reaction characteristics and mechanical properties of a commercial Al–20%Mg2Si–xCe in situ composite solidified at a slow cooling rate, J. Alloys Compd. 650 (2015) 821–834.

[25] B. Wan, W. Chen, L. Liu, X. Cao, L. Zhou, Z. Fu, Effect of trace yttrium addition on the microstructure and tensile properties of recycled Al–7Si–0.3Mg–1.0Fe casting alloys, Mater. Sci. Eng. A 666 (2016) 165–175.

[26] A.L. Greer, Overview: Application of heterogeneous nucleation in grain-refining of metals, J. Chem. Phys. 145 (21) (2016) 211704.

[27] A.L. Greer, P.S. Cooper, M.W. Meredith, W. Schneider, P. Schumacher, J.A. Spittle, A. Tronche, Grain refinement of aluminium alloys by inoculation, Adv. Eng. Mater. 5 (1–2) (2003) 81–91.

[28] A.L. Greer, Grain refinement of alloys by inoculation of melts, Philos. Trans. R. Soc. London. Ser. A Math. Phys. Eng. Sci. 361 (1804) (2003) 479–495.

[29] L. Lu, A.K. Dahle, Iron-rich intermetallic phases and their role in casting defect formation in hypoeutectic Al-Si alloys, Metall. Mater. Trans. A 36 (13) (2005) 819–835.

[30] X. Cao, J. Campbell, The nucleation of Fe-Rich phases on oxide films in Al-11.5Si-0.4Mg cast alloys, Metall. Mater. Trans. A 34 (7) (2003) 1409–1420.

[31] A. Lui, P.S. Grant, I.C. Stone, K.A.Q. O'Reilly, The Role of Grain Refiner in the Nucleation of AlFeSi Intermetallic Phases During Solidification of a 6xxx Aluminum Alloy, Metall. Mater. Trans. A 50 (11) (2019) 5242–5252.

[32] E. Liotti, C. Arteta, A. Zisserman, A. Lui, V. Lempitsky, P.S. Grant, Crystal nucleation in metallic alloys using x-ray radiography and machine learning, Sci. Adv. 4 (4) (2018) eaar4004.

[33] M.G. Tsoutsouva, G. Regula, B. Ryningen, P.E. Vullum, N. Mangelinck-Noël, G. Stokkan, Dynamic observation of dislocation evolution and interaction with twin boundaries in silicon crystal growth using in – situ synchrotron X-ray diffraction imaging, Acta Mater. 210 (2021) 116819.

[34] L. Abou-Khalil, K.S. da Cruz, G. Reinhart, N. Mangelinck-Noël, H. Nguyen-Thi, Influence of growth velocity on fragmentation during directional solidification of Al – 14 wt.% Sn alloy studied by in-situ synchrotron X-radiography, Acta Mater. 241 (2022) 118370.

[35] L. Abou-Khalil, Z. Thompson, G. Reinhart, T. Stan, L. Sturz, G. Zimmermann, P. W. Voorhees, N. Mangelinck-Noël, H. Nguyen-Thi, Three-dimensional investigation of fragment distribution in Al – 7wt.% Si solidified in microgravity, Acta Mater. 250 (2023) 118882.

[36] G. Reinhart, D. Grange, L. Abou-Khalil, N. Mangelinck-Noël, N. Niane, V. Maguin, G. Guillemot, C.-A. Gandin, H. Nguyen-Thi, Impact of solute flow during directional solidification of a Ni-based alloy: In-situ and real-time X-radiography, Acta Mater. 194 (2020) 68–79.

[37] E. Liotti, A. Lui, T. Connolley, P.S. Grant, Probing interdendritic flow and hot tearing during solidification using real time X-ray imaging and droplet tracking, Acta Mater. 240 (2022) 118298.

[38] S. Feng, E. Liotti, A. Lui, M.D. Wilson, T. Connolley, R.H. Mathiesen, P.S. Grant, In-situ X-ray radiography of primary Fe-rich intermetallic compound formation, Acta Mater. 196 (2020) 759–769.

[39] P.S. Mohanty, J.E. Gruzleski, Mechanism of grain refinement in aluminium, Acta Metall. Mater. 43 (5) (1995) 2001–2012.

[40] P. Schumacher, A.L. Greer, J. Worth, P.V. Evans, M.A. Kearns, P. Fisher, A.H. Green, New studies of nucleation mechanisms in aluminium alloys: Implications for grain refinement practice, Mater. Sci. Technol. 14 (5) (1998) 394–404.

[41] M. Easton, D. Stjohn, Grain refinement of aluminum alloys: Part I. The nucleant and solute paradigms - a review of the literature, Metall. Mater. Trans. A Phys. Metall. Mater. Sci. 30 (6) (1999) 1613–1623.

[42] Z. Fan, Y. Wang, Y. Zhang, T. Qin, X.R. Zhou, G.E. Thompson, T. Pennycook, T. Hashimoto, Grain refining mechanism in the Al/Al-Ti-B system, Acta Mater. 84 (2015) 292–304.

[43] S. Feng, E. Liotti, A. Lui, M.D. Wilson, P.S. Grant, Nucleation bursts of primary intermetallic crystals in a liquid Al alloy studied using in situ synchrotron X-ray radiography, Acta Mater. 221 (2021) 117389.

[44] H. Springer, R. Aparicio Fernandez, M.J. Duarte, A. Kostka, D. Raabe, Microstructure refinement for high modulus in-situ metal matrix composite steels via controlled solidification of the system Fe-TiB2, Acta Mater. 96 (2015) 47–56.

[45] Y. Cui, C. Gourlay, Growth twinning and morphology of Al45Cr7 and Al13Fe4, J. Alloys Compd. 893 (2022) 162318.

[46] P. Norby, A.N. Christensen, Preparation and structure of Al3Ti, Acta Chem. Scand. Ser. A 40 (1986) 157–159.

[47] J. Grin, U. Burkhardt, M. Ellner, K. Peters, Refinement of the Fe4Al13 structure and its relationship to the quasihomological homeotypical structures, Zeitschrift fuer Krist. 209 (6) (1994) 479–487.

[48] M.X. Zhang, P.M. Kelly, M.A. Easton, J.A. Taylor, Crystallographic study of grain refinement in aluminum alloys using the edge-to-edge matching model, Acta Mater. 53 (5) (2005) 1427–1438.

[49] P.M. Kelly, M.X. Zhang, Edge-to-edge matching–The fundamentals, Metall. Mater. Trans. A 37 (3) (2006) 833–839.

[50] Z. Fan, An epitaxial model for heterogeneous nucleation on potent substrates, Metall. Mater. Trans. A Phys. Metall. Mater. Sci. 44 (3) (2013) 1409–1418.

[51] T.B. Britton, D. Goran, V.S. Tong, Space rocks and optimising scanning electron channelling contrast, Mater. Charact. 142 (2018) 422–431.

[52] V.S. Tong, A.J. Knowles, D. Dye, T.B. Britton, Rapid electron backscatter diffraction mapping: Painting by numbers, Mater. Charact. 147 (2019) 271–279.

[53] J.W. Xian, L. Peng, G. Zeng, D. Wang, C.M. Gourlay, Al11Mn4 formation on Al8Mn5 during the solidification and heat treatment of AZ-series magnesium alloys, Materialia 19 (2021) 101192.

[54] M. Zhu, P. Wu, Q. Li, B. Xu, Vacancy-induced brittle to ductile transition of W-M co-doped Al3Ti (M=Si, Ge, Sn and Pb), Sci. Rep. 7 (1) (2017) 1–7.

[55] Y. Cui, D. King, A. Horsfield, C. Gourlay, Solidification orientation relationships between Al3Ti and TiB2, Acta Mater. 186 (2020) 149–161.

[56] R. Gupta, G.P. Chaudhari, B.S. Daniel, Effect of in-situ formed Al3Ti particles on the microstructure and mechanical properties of 6061 Al alloy, in: IOP Conf. Ser. Mater. Sci. Eng., Vol. 330, 2018, p. 012012.

[57] D.H. St, L.M. Hogan John, Metallography and growth crystallography of Al3Ti in Al-Ti alloys up to 5 wt% Ti, J. Cryst. Growth 46 (3) (1979) 387–398.

[58] G. Zeng, J. Xian, C. Gourlay, Nucleation and growth crystallography of Al8Mn5 on B2-Al(Mn, Fe) in AZ91 magnesium alloys, Acta Mater. 153 (2018) 364–376.

[59] J. Xian, S. Belyakov, M. Ollivier, K. Nogita, H. Yasuda, C. Gourlay, Cu6Sn5 crystal growth mechanisms during solidification of electronic interconnections, Acta Mater. 126 (2017) 540–551.

[60] Z.P. Que, Y.P. Zhou, Y. Wang, Z. Fan, Composition templating for heterogeneous nucleation of intermetallic compounds, in: Proc. of the 6th Decennial Intern. Conf. on Solidification Process. at Old Windsor, UK, 2017, pp. 158–161.

[61] K.F. Kobayashi, S. Hashimoto, P.H. Shingu, Nucleation of Aluminum by Al3Ti in the Al-Ti System, Zeitschrift fuer Met. Res. Adv. Tech. 74 (11) (1983) 751–754.

[62] Z. Chen, K. Yan, Grain refinement of commercially pure aluminum with addition of Ti and Zr elements based on crystallography orientation, Sci. Rep. 10 (1) (2020) 16591.

[63] J.H. Van Der Merwe, The role of lattice misfit in epitaxy, Crit. Rev. Solid State Mater. Sci. 7 (3) (1978) 209–231.

[64] M.X. Zhang, P.M. Kelly, Edge-to-edge matching and its applications: Part I. Application to the simple HCP/BCC system, Acta Mater. 53 (4) (2005) 1073–1084.

[65] F. Frank, J.H. Van Der Merwe, One-dimensional dislocations. II. Misfitting monolayers and oriented overgrowth, Proc. R. Soc. London. Ser. A. Math. Phys. Sci. 198 (1053) (1949) 216–225.

[66] J.H. Van Der Merwe, Crystal interfaces. Part I. Semi-infinite crystals, J. Appl. Phys. 34 (1) (1963) 117–122.

[67] L. Wang, L. Yang, D. Zhang, M. Xia, Y. Wang, J.G. Li, The Role of Lattice Misfit on Heterogeneous Nucleation of Pure Aluminum, Metall. Mater. Trans. A Phys. Metall. Mater. Sci. 47 (10) (2016) 5012–5022.

[68] S. Miyazaki, S. Kumai, A. Sato, Plastic deformation of a monoclinic Al13Fe4 at 300–873 K, Philos. Mag. 90 (19) (2010) 2597–2618.

[69] C.M. Adam, L.M. Hogan, Crystallography of the Al-Al3 Fe eutectic, Acta Metall. 23 (3) (1975) 345–354.

[70] X.L. Ma, H. Liebertz, U. Köster, Multiple twins of monoclinic Al13Fe4 showing pseudo-orthorhombic and fivefold symmetries, Phys. Status Solidi Appl. Res. 158 (2) (1996) 359–367.

[71] M. Ellner, Polymorphic phase transformation of Fe4Al13 causing multiple twinning with decagonal pseudo-symmetry, Acta Crystallogr. Sect. B 51 (1) (1995) 31–36.

[72] J.Y. Hwang, H.W. Doty, M.J. Kaufman, Crystallographic studies on the iron-containing intermetallic phases in the 319-type aluminium casting alloys, Philos. Mag. 88 (4) (2008) 607–619.

[73] A.L. Greer, A.M. Bunn, A. Tronche, P.V. Evans, D.J. Bristow, Modelling of inoculation of metallic melts: application to grain refinement of aluminium by Al-Ti-B, Acta Mater. 48 (11) (2000) 2823–2835.

[74] J. Rakhmonov, G. Timelli, F. Bonollo, L. Arnberg, Influence of grain refiner addition on the precipitation of fe-rich phases in secondary alsi7cu3mg alloys, Int. J. Metalcasting 11 (2) (2017) 294–304.

[75] Z. Fan, F. Gao, B. Jiang, Z. Que, Impeding Nucleation for More Significant Grain Refinement, Sci. Rep. 10 (1) (2020) 1–11.

[76] Y. Jia, H. Huang, Y. Fu, G. Zhu, D. Shu, B. Sun, D. StJohn, An in situ investigation of the solute suppressed nucleation zone in an Al-15Cu alloy inoculated by Al-Ti-B, Scr. Mater. 167 (2019) 6–10.